

MICROMECHANICAL FRACTURE MODELING FOR MECHANISTIC DESIGN OF THIN OVERLAYS

FINAL PROJECT REPORT

by

Hasan Ozer
Imad Al-Qadi
Jaime Hernandez
Mohammed Sawalha
Jose Rivera-Perez
University of Illinois at Urbana-Champaign

for

Center for Highway Pavement Preservation
(CHPP)



In cooperation with US Department of Transportation-Research and Innovative Technology
Administration (RITA)

April, 2018

Disclaimer

The contents of this report reflect the view of the authors, who are responsible for the facts and the accuracy of the data presented herein. The contents do not necessarily reflect the official views or policies of the Illinois Center for Transportation. This report does not constitute a standard, specification, or regulation. Trademark or manufacturers' names appear in this report only because they are considered essential to the object of this document and do not constitute an endorsement of product by the Illinois Center for Transportation.

Technical Report Documentation Page			
1. Report No. ICT-18-004	2. Government Accession No. N/A	3. Recipient's Catalog No. N/A	
4. Title and Subtitle Micromechanical Fracture Modeling for Mechanistic Design of Thin Overlays		5. Report Date April 2018	
		6. Performing Organization Code N/A	
7. Author(s) Hasan Ozer, Imad Al-Qadi, Jaime Hernandez, Mohammed Sawalha, Jose Rivera-Perez		8. Performing Organization Report No. ICT-18-004 UILU-ENG-2018-2004	
9. Performing Organization Name and Address CHPP Center for Highway Pavement Preservation, Tier 1 University Transportation Center Michigan State University, 2857 Jolly Road, Okemos, MI 48864		10. Work Unit No. (TRAIS) N/A	
		11. Contract or Grant No.	
12. Sponsoring Organization Name and Address United States of America Department of Transportation Research and Innovative Technology Administration		13. Type of Report and Period Covered Final Report 09/30/2013-09/30/2018	
		14. Sponsoring Agency Code	
15. Supplementary Notes Report uploaded at http://www.chpp.egr.msu.edu/			
16. Abstract Asphalt concrete responses to Illinois Flexibility Index Test (I-FIT) were studied using a micromechanical finite element model in order to explore the possibility of linking I-FIT results and overlay design. The model assumed AC composed of two phases: aggregate and mortar. Aggregate was considered linear elastic with material constants reported in the literature, while mortar was linear viscoelastic. Mortar was defined as the combination of binder, air voids, and material passing No. 8 (2.36 mm) sieve. Mixture theory was utilized to characterize mortar as viscoelastic using binder's dynamic shear rheometer results, elastic properties of fine material, and air voids volume from the mix design. Finally, mortar–aggregate interface was defined by springs with constants from the tensile adhesion test. The micromechanical finite element model was validated with strain fields measured using digital image correlation. The validated finite element model was used to perform a parametric study aimed at determining the effect of gradation and binder properties on the reaction load, opening strains and stresses, and energy around the crack tip. Nine gradations and three binders were studied; ten replicates for each gradation-binder combination were made. In order to create the replicates, a Python script that fabricates artificial gradations and randomly distributes aggregates in the I-FIT geometry was created. It was found that mortar properties, rather than air voids, binder content, or fine material, were heavily correlated to energy and applied load of the I-FIT sample.			
17. Key Words I-FIT, micromechanical modeling, finite elements, digital image correlation, fracture properties, mortar		18. Distribution Statement No restrictions.	
19. Security Classification (of this report) Unclassified.	20. Security Classification (of this page) Unclassified.	21. No. of Pages 49 pp.	22. Price N/A

Table of Contents

CHAPTER 1 - INTRODUCTION.....	1
1.1 BACKGROUND.....	1
1.2 OBJECTIVE AND SCOPE.....	2
1.3 RESEARCH APPROACH.....	2
1.4 OVERVIEW OF THE REPORT	3
CHAPTER 2 - LITERATURE REVIEW.....	4
CHAPTER 3 - FRACTURE CHARACTERIZATION OF OVERLAY MIXES	8
3.1 GEOMETRY AND LOAD CONFIGURATION	8
3.2 MATERIAL PROPERTIES.....	9
3.2.1 Asphalt Binder	9
3.2.2 Aggregate.....	10
3.2.3 Mortar	12
3.2.4 Mortar-Aggregate Interface	16
3.3 CONTINUUM FRACTURE TEST MODEL.....	18
3.4 MICROMECHANICAL FRACTURE TEST MODEL.....	19
CHAPTER 4 - MODEL CALIBRATION AND VALIDATION	20
4.1 DIGITAL IMAGE CORRELATION	20
4.2 CALIBRATION OF THE CONTINUUM I-FIT FE MODEL	21
4.3 VALIDATION of MICROMECHANICAL FE MODEL	24
4.3.1 Image Processing	24
4.3.2 Image Thresholding and Segmentation.....	24
4.3.3 Comparison between Measured and Calculated Strains	26
CHAPTER 5 - EVALUATION OF MICROSTRUCTURAL FACTORS AFFECTING FRACTURE OF ASPHALT MIXES	29
5.1 COMPUTER-GENERATED FRACTURE TEST SPECIMENS	29
5.2 FRACTURE RESPONSE TO LOADING.....	34
5.2.1 Gradation Effect.....	35
5.2.2 Mortar Effect.....	40
5.3 Design Considerations.....	43
CHAPTER 6 - CONCLUSIONS AND RECOMMENDATIONS.....	45
REFERENCES	46

List of Figures

Figure 3-1 Load–displacement curve resulting from the I-FIT (AASHTO 2016).	9
Figure 3-2 Relaxation shear modulus of studied binders.	12
Figure 3-3 Dynamic shear modulus, phase angle, shift factor, storage shear modulus, loss shear modulus, and relaxation shear modulus for binder PAV N90-30.....	13
Figure 3-4 Determination of mortar relaxation modulus.....	15
Figure 3-5 Relaxation modulus of binder, mortar, and Prony series fit for mortar relaxation modulus.....	16
Figure 3-6 Tensile adhesive method fixture in the bath before testing.....	16
Figure 3-7 Tensile adhesive method fixture after failing.....	17
Figure 3-8 Failed specimen.....	17
Figure 3-9 Sample of adhesion test between binder and aggregate.....	18
Figure 3-10 Linear elastic homogeneous I-FIT model.	18
Figure 4-1 LDPE sample under I-FIT.....	21
Figure 4-2 Global load–displacement curve for LDPE specimen.	22
Figure 4-3 Comparison of ϵ_{11} between DIC measurements and ABAQUS results.....	23
Figure 4-4 Processing of images taken from a digital camera.....	24
Figure 4-5 Different phases defined in the Simpleware image segmentation (Ghauch et al. 2015).	25
Figure 4-6 Typical functioning window in Simpleware.	25
Figure 4-7 Mesh generated in Simpleware.	26
Figure 4-8 I-FIT load–displacement curve used for validation.	26
Figure 4-9 Comparison between measured and calculated opening strains in micromechanical model at carious loadings.....	27
Figure 5-1. Sample of Voronoi tessellations.....	29
Figure 5-2 Sample of computer-generated I-FIT specimen.....	30
Figure 5-3 Gradation of selected aggregate structures.	31
Figure 5-4 Sample of resulting images from Python script for each mix.	33
Figure 5-5 Mortar ratio and <i>VMA</i> for the nine mixes.	34
Figure 5-6 Location of paths for variation of σ_{11} and ϵ_{11}	35
Figure 5-7 Shear relaxation modulus for binder PG 64-22 RTFO and resulting mortars in Mixes 1 through 9 (reference temperature: 15 °C).	35
Figure 5-8 Shear relaxation modulus at $t=1.0$ s and <i>P16</i> for studied mixes.	36
Figure 5-9 Variation of load applied by the loading head and mortar stiffness at $t=1.0$ for each mix.	37
Figure 5-10 Variation of ϵ_{11} along Path 1 for Replicate 1 in all mixes.....	38
Figure 5-11 Variation of σ_{11} along Path 1 for Replicate 1 in all mixes.	39
Figure 5-12 Variation of energy term and mortar stiffness at $t=1.0$ for each mix.	40
Figure 5-13 Mortar relaxation modulus for the study of binder effect.	41
Figure 5-14. Variation of applied force with binder type for Mixes 4, 5, and 9.....	42
Figure 5-15 Variation of energy term and mortar stiffness at $t=1.0$ for each mix–binder combinations.	43
Figure 5-16. Variation of energy term and applied force for each mix–binder combinations.	43

List of Tables

Table 3-1 Relaxation Times and Prony Terms for Binders in Categories 1 and 2	10
Table 3-2 Relaxation Times and Prony Terms for Binders in Category 3	11
Table 3-3 Relaxation Times and Prony Terms for Binders in Category 3 after PAV Aging	11
Table 5-1 Gradation, Binder Content, and VMA of Selected Aggregate Structures.....	32
Table 5-2. Prony Series Terms for Mortars	40
Table 5-3. Summary of Energy and Force for the Various Mix–Binder Combinations.....	44

List of Abbreviations

CHPP: Center of Highway Pavement Preservation

MDOT: Michigan Department of Transportation

Table of Abbreviations

AASHTO	American Association of State Highway, & Transportation Officials
AI	Asphalt Institute
CR	Crumb rubber
DCT	Disc-Shaped Compact Tension Test
DIC	Digital image correlation
DSR	Dynamic shear rheometer
FE	Finite element
FHWA	Federal Highway Administration
LEFM	Linear elastic fracture mechanics
NCHRP	National Cooperative Highway Research Program
PANDA	Pavement Analysis Using Nonlinear Damage Approach
PPA	Poly phosphoric acid
RAP	Reclaimed asphalt pavement
RAS	Recycled asphalt shingles
RITA	Research and Innovative Technology Administration
RRD	Representative rebound deflection
SBS	Styrene butadiene styrene
SCB	Semi-circular beam
SENB	Single-edge notched beam
SIF	Stress intensity factor
TFHRC	Turner-Fairbank Highway Research Center

Acknowledgments

The authors would like to acknowledge the financial support of the Center for Highway Pavement Preservation and the US Department of Transportation-Research and Innovative Technology Administration (RITA).

Executive Summary

Asphalt concrete (AC) overlays are one of the most common preservation techniques of road infrastructure; however, none of the existing procedures used to determine overlay thickness are fully mechanistic. The three main approaches currently used for overlay design are AASHTO, deflection-based, and mechanistic-empirical methods. The AASHTO method determines overlay thickness by calculating the structural number needed for an existing pavement to withstand future traffic. The deflection-based method, which is recommended by the Asphalt Institute, correlates properties of existing pavement and measurements of surface deflection to overlay thickness. Finally, the method incorporated in the mechanistic-empirical pavement design guide calculates the structural responses using multi-linear layered elastic models and damage from empirically derived transfer functions.

Development of fully mechanistic methods to determine the thickness of AC overlays poses numerous challenges. First, cracking is considered the main failure mechanics of overlays. Fracture mechanics provide closed-form solutions for displacement and stresses around the crack tip for very specific geometries and loading conditions, none of which resembles a pavement. Even more, the overlay's structural response depends on factors usually omitted in the conventional analysis of pavements such as accurate tire-pavement contact area and non-uniform three-dimensional contact stresses. Another more computationally efficient approach would be to link the fracture properties of AC measured in the laboratory with the mechanical responses of a three-dimensional continuous pavement model.

Numerous tests can be used to study AC's fracture behavior, but the Illinois Flexibility Index Test (I-FIT), used in this study, provides advantages such as easy sample preparation and good quality data. I-FIT was modeled using the finite element (FE) method, considering AC composed of two phases: mortar and aggregate. Aggregate was assumed linear elastic with material constants obtained from the literature. Mortar's material characterization was more elaborate. First, it was linear viscoelastic consisting of aggregates passing No. 8 (2.36 mm) sieve, air voids, and binder. Mortar's material constants were calculated using dynamic shear rheometer (DSR) results from the binder, and air voids information and fine aggregate volume from the mix design. The micromechanical FE model was validated comparing numerical predictions with strain fields measured using digital image correlation. In addition, a continuous FE model of I-FIT was also developed and validated as an initial approach to link road responses from a continuous three-dimensional pavement model and micromechanical I-FIT FE model.

Two main AC variables were studied: binder properties and aggregate gradation. Nine mix designs and three asphalt binders were included in the numerical analysis matrix. For each gradation-binder combination, ten replicates were created using a Python script that randomly placed the aggregate satisfying a specific gradation on the I-FIT sample. Ten outcomes of the FE model were used to study the AC behavior: applied load, opening strains and stresses, and energy. Due to the heterogeneity caused by aggregate distribution, it was found that the opening strains/stress along specific paths on the I-FIT sample were not a reliable comparison benchmark. On the other hand, the applied load and energy exhibited small variation among samples of a specific aggregate-binder combination. The numerical analysis matrix also showed that applied load and energy did not correlate with air voids, binder, and/or fine material.

However, the two outcomes properly correlate with mortar modulus because it is affected by the three variables simultaneously (air voids, mortar, and fine material). This finding also indicates that when designing a material for a thin overlay, special attention should be given to the interaction between binder, fine material, and air voids rather than each one of these components individually.

CHAPTER 1 - INTRODUCTION

1.1 BACKGROUND

According to the American Society of Civil Engineers (ASCE), 32% of major roads in the United States are in poor or mediocre condition (ASCE 2017). Asphalt concrete (AC) overlays have become a popular pavement preservation technique because they provide more benefits than other techniques such as: i) long service life and low life-cycle assessment, ii) grade and slope preservation with minimal impact on drainage; iii) smooth surface without loose aggregates; iv) minimal delay before road opening; and v) low noise generation, among others (Newcomb 2009).

Even though there are commonly used procedures for determining overlay thickness, none of them is fully mechanistic. For instance, the effective thickness method relies on the AASHTO design formula to find the additional thickness needed to satisfy future traffic demands according to the current state of pavement (AASHTO 1993). The deflection-based method relates deflections measurements, traffic, and stiffness of existing pavement to overlay thickness (AI 2000). The most advanced overlay design procedure is probably the mechanistic-empirical method (MEPDG 2004). This procedure calculates pavement overlay responses from the multilayer elastic methods and uses empirical functions to relate such responses to overlay damage.

In fully mechanistic methods for overlay design, material testing and characterization should be directly linked to the calculation of pavement responses and overlay thickness. Mechanistic analysis of overlays poses several challenges. Three-dimensional and non-uniform contact in addition to aging and temperature gradients generate a complex 3-D stress and strain fields. In addition, the microstructure of asphalt mixture can govern the responses within a thin overlay under such complex 3-D stress/strain field. Therefore, conventional mechanistic methods and critical response parameters fail to represent such complexities. Material characterization representative of the conditions governing the response of overlays and advanced structural analysis methods are needed to understand mechanics of overlays.

The main failure mechanism of AC overlays is fracture, so it becomes necessary to accurately characterize the fracture performance of AC due thermal fluctuations and movements in the underlying layers. Several tests have been used to determine such characterization (e.g., single-edge notched beam, disc-shaped compact tension test, beam fatigue, etc.), but the semi-circular beam (SCB), I-FIT in particular, provides the most advantages regarding sample preparation, data quality, equipment needed to perform the test, and testing time.

Despite the use of SCB for fracture characterization of AC mixture, a clear computational efficient and practical link have not been established between laboratory testing and the analysis of AC overlays. Most links are based on linear elastic fracture mechanics (i.e., AC is assumed linear elastic and homogenous material) and require the inclusion of cracks in the pavement model. Including cracks in the calculation of pavement responses considerably increases the computational time of pavement responses and may raise convergence issues.

Therefore, there is a need for an overlay design method based on a mechanistic analysis considering AC mixes microstructure and cracking response along with an appropriate method of pavement analysis capturing complex near-surface stress and strain fields. Volume I and Volume II of the report present an alternative mechanistic analysis of thin overlays as follows:

- Volume I: Micromechanical characterization of cracking of mixes used in asphalt overlays
- Volume II: Mechanistic analysis of pavements with overlays considering microstructural features

1.2 OBJECTIVE AND SCOPE

The main objective of this study is to develop a micromechanical analysis method for AC mixture with results that can be fed into the design of AC overlays. The micromechanical analysis is proposed to bridge the microstructural response of AC mixtures to the overlay characterization in the global scale under traffic loading conditions. Since it is computationally prohibitive to consider microstructural features explicitly in the analytical or numerical simulations of pavements, the objective of this study is to accomplish the following goals:

- Develop a method to evaluate critical key parameters governing cracking response of mixtures through micromechanical test scale simulations
- Calculate microstructure-based mixture characteristics that can be used in pavement structural analysis for overlays

1.3 RESEARCH APPROACH

To accomplish the study goals, a micromechanical FE model of the I-FIT was developed to quantify the effect of primary microstructural features that may affect crack initiation and propagation, such as mix design variables and material properties. The model results include critical stress/strain based parameters as well as energy-based variables linking I-FIT results and failure of AC overlays.

The research approaches and procedures in the project include the following:

- Compile multiple mix designs covering a wide range of applications (gradations, binder contents, voids in the mineral aggregate, etc.) to study the pavement responses when subjected to I-FIT micromechanical FE model
- Create a Python-based algorithm to generate digital I-FIT samples using gradation and volumetric information as input variables
- Develop a two-phase micromechanical FE model of the I-FIT test that considers aggregate distribution, viscoelasticity caused by asphalt binder, and displacement-controlled loading
- Determine aggregate–mortar interface properties through laboratory testing to be used as input in the FE model
- Determine viscoelastic characterization of asphalt mortar based on rheological properties of asphalt binder and amount of small aggregate in the mixture

- Study the effect of mix design, gradation, and mortar properties on I-FIT responses: applied load, stresses, and strain, among others.

1.4 OVERVIEW OF THE REPORT

The body of the report is divided into six chapters. Chapter 2 provides an overview of the I-FIT test from the laboratory and modeling points of view in addition to a summary of current overlay design approaches used by practitioners. Chapter 3 presents the I-FIT FE model and inputs such as material characterization, geometry, and loading. Chapter 4 illustrates experimental techniques used to verify validity of the FE model and how they were used. In Chapter 5, application of the FE model to typical AC mixtures and corresponding I-FIT responses are analyzed. Chapter 6 provides the study's conclusions and recommendations.

CHAPTER 2 - LITERATURE REVIEW

Traditionally, three approaches have been used to design overlays: effective thickness, deflection, and the mechanistic-empirical approach. The AASHTO method uses the effective thickness approach, where the overlay thickness depends on the capacity of existing pavement and the required capacity imposed by future traffic (AASHTO 1993). Overlay thickness is calculated as the ratio between the difference in the structural number required to carry future traffic and the effective structural number of existing pavement over the structural coefficient of the AC overlay. The deflection approach relies on nondestructive testing (NDT) and the representative rebound deflection (RRD) (AI 2000). RRD can be directly measured using the Benkelman beam or correlated to other NDT measurements. The overlay thickness can be determined using the relationships between *ESAL*, modulus of existing pavement, and RRD. Finally, the mechanistic-empirical (M-E) design methodology, as in the case of new pavements, relies on the calculation of pavement responses and their relationships to distresses through transfer functions (MEPDG 2004).

Recent research efforts on the design of overlays mostly focus on improving M-E methodologies. For instance, Sousa and co-authors (Sousa et al. 2002, 2005) developed a FE model using SAP2000 that was calibrated with measurements of cracked pavements. The laboratory component determined the flexural fatigue life of AC, and the analytical component (FE model), which included a crack, provided crack activity in the vertical direction. An M-E overlay design procedure was proposed, but its applicability is limited to very specific site conditions (Sousa et al. 2002). Al-Qadi et al. derived design equations to predict overlay service life against reflective cracking with and without steel reinforcements (Al-Qadi et al. 2003). Cracks were considered in the model by creating singularities in the FE mesh around the crack tip. Two stages were considered: crack initiation and crack propagation. Crack initiation was calculated using transfer functions and crack propagation was based on a relationship between stress intensity factor (SIF) and crack length derived from the FE model.

Even though the M-E procedure represents an improvement compared with purely empirical approaches, such as the effective thickness method, it has limitations that can be overcome using purely mechanistic methods. For instance, transfer functions are valid only for the conditions under which they are established, and their development requires considerable experimental resources. Two studies can be cited as samples of purely mechanistic methods. In 1995, Collop and Cebon explained the fatigue cracking mechanism of flexible pavements using linear elastic fracture mechanics (Collop and Cebon 2005). The plane-strain, two-dimensional (2-D) analysis utilized Von Mises criteria to calculate the fracture process zone size, and the FE model assumed the pavement as a thin plate; this assumption allowed the use of closed-form expression for the SIF to calculate stresses. This study does not precisely focus on AC overlays, but rather highlights the importance of establishing a link between the fracture properties of pavement materials and pavement responses.

More recently, fatigue cracking was included in the Pavement Analysis Using Nonlinear Damage Approach (PANDA) by adding cohesive zone fracture law (You et al. 2016). Viscoelastic, viscoplastic, and rate-dependent damage was incorporated in ABAQUS with material properties from laboratory testing. In the case of fracture, the performed test was the

third-point semi-circle beam (SCB) at room temperature. The fracture parameters of the cohesive model were determined through calibration process that matched experimental measurements from SCB and a three-dimensional (3-D) homogenous FE model. The link between the fracture properties and pavement model was established using rate-dependent damage material properties and damage evolution function. Finally, a 2-D pavement model was used to analyze the response of thin overlays.

The aforementioned studies emphasized the relevance of fracture properties of AC on the cracking analysis of flexible pavements. In addition, cracking is also known to be one of the main failure mechanisms of AC overlays, making even more relevant the understanding of AC fracture behavior. SCB has been instrumental for gaining such understanding because it provides several advantages compared with other fracture tests. Some of the advantages include easy sample preparation and testing, good quality and repeatability of test results, shorter testing time, and the lack of need for new testing equipment.

Artamendi and Khalid compared SIF and fracture energy of AC using the single-edge notched beam (SENB) and SCB tests (Artamendi and Khalid 2006). The tests were performed on Mode I and Mix-Mode I/II, and a small difference in SIF was found. However, SCB provided significantly higher fracture energy, generated higher stresses, and sustained a higher load than SENB. SCB was also compared with the disc-shaped compact tension test (DCT). For instance, using SCB and DCT, the effect of binder, binder modifier, aggregate type, asphalt content and air voids on the fracture performance of AC was studied (Li et al. 2008). The tests were performed at low temperature, and the influence of aggregate type on fracture energy was reported. Regarding air voids, SCB showed higher fracture energy for samples with 4 % air voids compared with samples having 7 % air voids (lower air voids demonstrated higher fracture resistance). On the contrary, DCT presented higher variability and opposite trend. Even more, DCT did not capture the influence of air voids on fracture properties. As for binder content, no significant effect was observed on SCB results, and it was concluded that a high binder content does not necessarily result in higher crack resistance. Based exclusively on the results obtained from low-temperature SCB tests, a reduction in fracture energy was reported with decreasing loading rates (Li and Marasteanu 2010).

SCB was also compared with the indirect tensile strength (IDT) test (Mohammad et al. 2008). The same mix design using three different binders was tested at two temperatures, 25 and 40 °C. SCB results provided lower critical strain energy for the aged mix, while IDT ranked mixtures differently depending on the criteria used (strength, strain, or toughness index). Both tests provided good correlation between their corresponding parameters (i.e., between toughness index from IDT and critical J -integral from SCB). Similarly, Kim and co-authors used SCB and IDT at room temperature to determine the influence of mix type (warm and hot AC), binder grade, aging, and reclaimed asphalt pavement on the fracture parameters (Kim et al. 2012). Two main outcomes can be inferred from this study: i) fracture energy increases by polymer-modified binder, decreases with aging, and is neither affected by lower mixing temperatures nor RAP contents up to 30%; ii) there is a good correlation between the critical J -integral from SCB test and cracking performance of flexible pavements at intermediate temperatures.

In many cases, SCB has been used as the only tool for evaluating the fracture performance of AC mixtures. In 2006, Li and Marasteanu used SCB at low temperatures to study the behavior of the same mix with different binders (Li and Marasteanu 2006). A direct relationship between temperature and fracture energy was reported; however, a clear and uniform trend was not found for the critical SIF and the various binders (the ranking changed with temperature). Using the variation between the applied load and crack mouth opening displacement, the fracture performance of various AC mixes [ten conventional dense-graded, four polymer-modified gap-graded (PGAP), four rubber-modified gap-graded (ARGAP), and one rubber-modified open-graded (AROP) mixes] was evaluated. The critical SIF of dense-graded mixes was higher, while ARGAP provided the highest dissipated fracture energy.

The SCB sample was modified to capture the mixed mode of fracture (Mixed Mode I/II). Pirmohammad and Ayatollahi used this modified configuration to test normal and modified mixes at low temperature and find the SIF (Pirmohammad and Ayatollahi 2014). Different fracture modes were obtained by changing the distance from the center of the notch to the supports: the symmetric distance provided a pure Mode I; the supports next to the notch resulted in a pure Mode II; and the asymmetric distance defined mixed mode I/II. In general, it was concluded that the modified mix is more crack resistant than the normal mix and that the effect of temperature on the SIF is not uniform for the range tested (increased from -35°C to -20 °C and then decreased for values higher than -20 °C). Aliha et al. also used Mode I, Mode II, and Mixed Mode I/II, for evaluating four binder modifiers [poly phosphoric acid (PPA), styrene butadiene styrene (SBS), anti-stripping agent, crumb rubber (CR) and F-T paraffin wax (Sasobit)] in addition to the unmodified AC mix (Aliha et al. 2015). The study reported an increase in fracture toughness caused by modifiers, and, as in the previous studies, the effect of temperature was not consistent for the range of temperatures tested (-30, -22, -15 °C). Furthermore, the fracture toughness also increased when air voids decreased from 7 to 3%, but the ranking of the various modifiers was not the same (Aliha et al. 2015). The mixed mode fracture was also studied using FE modeling (Aliha et al. 2012, Ameri et al. 2012). The model allowed the prediction of geometric factors for the calculation of SIF, assuming that the material is linear elastic homogenous isotropic.

FE modeling was also part of research efforts aimed to understand the fracture behavior of AC. FE models and experiments were used to compare SENB and SCB based on linear elastic fracture mechanics (Abu Abdo et al. 2014). The result showed no significant difference between both tests configurations; good correlation was also observed between the experiment and model for the critical SIF and maximum tensile stress. A more extensive comparison was performed by Aragoño and et al., who compared SCB, SENB, and DCT using FE (Aragoño et al. 2014). The model considered viscoelasticity and cohesive elements with parameters determined through calibration and experimental measurements. Material characterization was acquired testing fine aggregate mixes; small cylinders for viscoelastic characterization and fracture samples were obtained from the same mixture core. The study reported insignificant variation in fracture properties, most likely due to the use of fine mixes. The effect of RAP content on fracture behavior was the target of laboratory testing and numerical modeling of SCB. Mixtures with RAP content of 0, 15, and 40% were subjected to a loading rate of 0.5 mm/min. The numerical model was three-dimensional, included a bi-linear cohesive zone element and homogenous

isotropic viscoelastic material. Calibration was performed using the experimental results, which were able to capture the higher brittleness caused by RAP (Elseifi et al. 2015).

Fatigue loading was applied to the SCB configuration (Huang et al. 2013). The numerical model advanced the support conditions by assuming frictionless hard contact with rigid surfaces in a 2-D homogenous model. LEFM was utilized to determine SIF and established the Paris' law for the mixtures analyzed. It was concluded that asphalt binder plays a major role on the fracture performance of AC mixtures.

In summary, the SCB test plays an instrumental role in the mechanistic analysis of fracture performance of AC mixtures, which is relevant for the calculation of responses and design of AC overlays. However, there is a gap between the results provided by the SCB test and the analysis of flexible pavements. Furthermore, most research efforts make inappropriate assumptions for the material behavior of AC because the heterogeneous nature of AC is usually omitted, even when considering viscoelasticity. The Illinois Center for Transportation has adopted the SCB geometry and fine-tuned the testing condition to characterize the fracture behavior of AC (Al-Qadi et al. 2015, Ozer et al. 2016, 2016b). A DIC technique with a very high-resolution camera was used to calculate the microstructural level strains developed at the crack tip of I-FIT specimens for various types of AC mixes (Doll et al. 2017, Ozer et al. 2016, Ozer et al. 2017). The effect of temperature, loading rate, and AC mix properties was investigated. This research builds on our earlier work by adding micromechanical FE modeling. The micromechanical FE model of the I-FIT was developed to quantify the effect of primary microstructural features that may affect crack initiation and propagation such as aggregate gradation variables and material properties.

CHAPTER 3 - FRACTURE CHARACTERIZATION OF OVERLAY MIXES

The Illinois Flexibility Index Test (I-FIT), which uses the SCB geometry, was selected to determine the fracture properties of mixes commonly used in overlays. The test is standardized by AASHTO TP 124-16 and is performed at room temperature; it provides the fracture energy and parameters from the load–displacement curve to compute the flexibility index (FI). The FI correlates with AC mixtures resistance to damage.

Fracture characteristics of the AC mixtures considered were determined based on the material before reaching the peak load. Special attention was given to the stresses, strains, energy, and applied force. This approach has two advantages: i) it does not require the inclusion of damage and/or plasticity on material characterization; and ii) it allows the creation of a link between the responses in I-FIT and a pavement model (presented in Volume II) based on linear viscoelasticity.

The main features of the modeling approach will be described in this chapter. First, geometry and load configuration of the I-FIT will be presented. Second, characterization of four components of the FE model (binder, mortar, aggregate, and mortar–aggregate interface) will be detailed. The chapter concludes by describing two I-FIT FE models along with their corresponding validation, one assuming linear elastic homogenous isotropic materials and the other micromechanical materials consisting of aggregate and mortar.

Each material assumption has its own purpose. On one hand, the continuum material assumption is used to perform a parametric study where the J -integral is calculated, and a relationship between J -integral, load, and elastic moduli are obtained. The relationship has the potential of linking continuous pavement and micromechanical I-FIT models using equivalent materials and correspondence principle. On the other hand, micromechanical I-FIT model is utilized to determine the effect of mix design variables on the fracture behavior of I-FIT.

3.1 GEOMETRY AND LOAD CONFIGURATION

The AASHTO TP 124-16 test was performed at room temperature on a semi-circular sample with a diameter of 150 mm, thickness of 50 mm, and notch depth of 15 mm. The notch was located at the center of the sample and was oriented at 90 degrees with respect to the bottom of the configuration (parallel to the line of loading). The specimen was supported by two steel rollers with a diameter of 25 mm and a center-to-center separation of 120 mm.

After a 0.1 kN contact load is applied, a loading head with a radius of 12.5 mm transferred a line-load displacement at a rate of 50 mm/min on top of the specimen until the load dropped below 0.1 kN. Figure 3-1 presents the typical variation of the recorded load P and line-load displacement u . The area under the curve defined the work of fracture, and the fracture energy resulted from dividing the work of energy by the ligament area. Finally, the flexibility index FI is obtained by dividing the fracture energy by the absolute value of the slope of post-peak tangent crossing the inflection point. Instead of using the fracture parameters described above,

this study focuses on the responses (stresses, strains, and deflection) around the notch area before reaching the peak load.

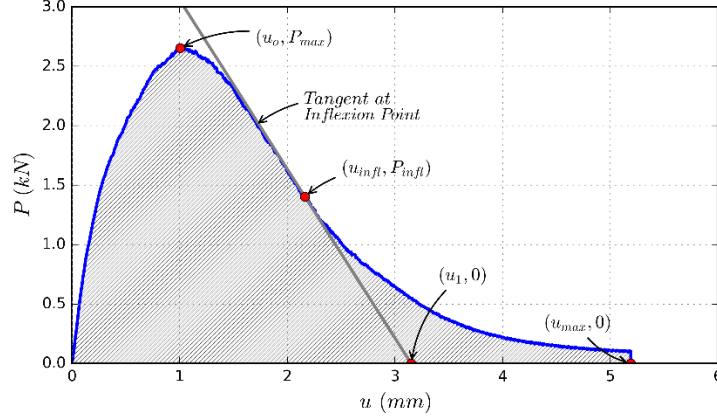


Figure 3-1 Load–displacement curve resulting from the I-FIT (AASHTO 2016).

3.2 MATERIAL PROPERTIES

To develop a micromechanical model, the AC microstructure is simplified to aggregate and mortar phases. Aggregate constitute the solid phase of AC with particle larger than No.8 (2.36 mm) sieve size. Mortar is defined as the combination of binder, air, and aggregates passing No. 8 (2.36 mm) sieve. In addition, the interaction between aggregate and mortar is defined using nonlinear springs to allow imperfect bonding conditions. Details of the material models for each component and the procedure followed to obtain the material constants are detailed in the following subsections.

3.2.1 Asphalt Binder

Asphalt binder characterization was not directly used in the FE modeling, but served as basis for the linear viscoelastic characterization of mortar. Asphalt binder was assumed linear viscoelastic, with relaxation shear modulus given by:

$$G(t) = G_e + \sum_{i=1}^n G_i e^{-t/\tau_i} = G_o - \sum_{i=1}^n G_i [1 - e^{-t/\tau_i}] \quad (3.1)$$

where: $G(t)$: shear relaxation modulus,
 G_e : equilibrium (long-term) modulus,
 $G_o = G_e + \sum_{i=1}^n G_i$: instantaneous modulus,
 G_i : relaxation strengths (Prony series terms),
 τ_i : relaxation times, and
 t : time.

The parameters G_i and τ_i were determined using frequency sweep test and dynamic shear rheometer (DSR) at various temperatures.

Seventeen binders were considered and grouped in three categories; material properties were obtained from the previous project databases as follows:

- The first category consists of three PG 64-22 binders aged at three levels using rolling thin film oven (RTFO), pressure aging vessel (PAV), and double PAV (Sharma et al., 2016). The label of these binders represents their PG-grade and the aging condition. Binder RTFO PG 64-22 with grade PG 64-22 was subjected to RTFO aging.
- Four binders belong to the second category and were used in the construction of pavement sections in the accelerated loading facility of the Turner-Fairbank Highway Research Center (TFHRC) of the Federal Highway Administration (FHWA). These binders, which were aged using the RTFO procedure, were labeled B-6602 RTFOT MC, B-6604 RTFOT MC, MC B-6603 RTFOT, and MC B-6605 RTFOT.
- The third and final category groups extracted asphalts with various levels of binder replacement (RAS and RAP); the amount of replacement and aging condition is indicated in the binder label (Al-Qadi et al., 2015). For instance, PAV N90-30 represents a binder extracted from a mixture designed for 90 gyrations containing 30% binder replacement aged following the PAV procedure. Ten binders belong to this category.

All binders were subjected to the frequency sweep test and DSR at various temperatures to measure the dynamic shear modulus $|G^*|$ and phase angle ϕ to properly characterize them as linear viscoelastic. Table 3-1 through Table 3-3 present the Prony series terms and relaxation times of the relaxation shear modulus of each binder. In addition, Figure 3-3 details the viscoelastic testing and results for one of the binders (PAV N90-30). From the top left to the bottom right, the figure shows the change of: i) dynamic shear modulus $|G^*|$ with the reduced frequency ξ ; ii) phase angle ϕ with dynamic shear modulus; iii) logarithm of the shift factor with respect to temperature; iv) storage shear modulus with reduced frequency; v) loss shear modulus with reduced frequency; and vi) relaxation shear modulus with reduced time t . Figure 3-2 compiles the relaxation shear modulus of the 17 considered binders.

3.2.2 Aggregate

Aggregates in the AC mixture were assumed linear elastic. No test was performed to determine elastic modulus and Poisson's ratio, but values reported in the literature were selected. In general, the elastic modulus of aggregates used in the production of AC varies between 20 and 80 GPa depending on the original rock type. The elastic modulus of the aggregate was considered 60 GPa for this study.

Table 3-1 Relaxation Times and Prony Terms for Binders in Categories 1 and 2

τ_i	Category 1			Category 2			
	PG64-22 RTFO	PAV PG64-22	2PAV PG64-22	B-6602 RTFOT MC	B-6604 RTFOT MC	MC B-6603 RTFOT	MC B-6605 RFTOT
0.00001	0.00E+00	0.00E+00	2.40E+03	1.09E+02	1.97E+02	1.06E+02	1.12E-01
0.0001	1.53E+02	3.91E+02	0.00E+00	2.24E+01	4.92E+01	2.13E+01	5.00E-02
0.001	5.40E+01	2.60E+01	4.84E+01	1.18E+01	3.19E+01	1.09E+01	2.65E-02
0.01	2.44E+01	2.87E+01	3.52E+01	3.43E+00	1.11E+01	2.89E+00	9.10E-03
0.1	1.03E+01	1.62E+01	2.27E+01	8.15E-01	3.19E+00	7.70E-01	2.51E-03
1	2.20E+00	6.63E+00	1.10E+01	1.23E-01	4.42E-01	9.68E-02	3.48E-04

10	4.38E-01	1.97E+00	4.54E+00	1.30E-02	8.99E-02	2.38E-02	7.92E-05
100	3.33E-02	4.50E-01	1.34E+00	0.00E+00	0.00E+00	0.00E+00	0.00E+00
1000	9.54E-03	7.32E-02	3.27E-01	0.00E+00	0.00E+00	0.00E+00	2.69E-07
10000	0.00E+00	1.32E-02	1.04E-01	0.00E+00	0.00E+00	0.00E+00	0.00E+00
100000	2.07E-03	0.00E+00	1.09E-02	0.00E+00	0.00E+00	0.00E+00	0.00E+00

Table 3-2 Relaxation Times and Prony Terms for Binders in Category 3

τ_i	Category 3				
	N90-10	N90-20	N90-30	N90-0 AS	N90-60 AS
0.00001	7.90E+02	3.65E+03	5.41E+03	9.96E+02	3.06E+03
0.0001	2.51E+01	0.00E+00	0.00E+00	0.00E+00	1.28E+02
0.001	4.97E+01	0.00E+00	0.00E+00	6.02E+01	0.00E+00
0.01	2.19E+01	1.89E+01	2.07E+01	2.63E+01	2.03E+01
0.1	1.05E+01	8.81E+00	1.43E+01	1.28E+01	1.20E+01
1	2.93E+00	3.61E+00	5.51E+00	3.75E+00	5.60E+00
10	6.57E-01	8.36E-01	1.63E+00	7.52E-01	2.02E+00
100	9.07E-02	2.26E-01	3.12E-01	1.26E-01	5.71E-01
1000	1.28E-02	3.09E-02	7.13E-02	7.68E-03	1.61E-01
10000	3.67E-04	5.23E-03	6.62E-03	0.00E+00	3.64E-02
100000	3.27E-04	0.00E+00	0.00E+00	0.00E+00	4.31E-03

Table 3-3 Relaxation Times and Prony Terms for Binders in Category 3 after PAV Aging

τ_i	Category 3 - PAV				
	PAV N90-0AS	PAV N90-30	PAV N90-10	PAV N90-20	PAV N90-60AS
0.00001	2.72E+03	0.00E+00	0.00E+00	1.62E+03	0.00E+00
0.0001	0.00E+00	2.31E+02	2.13E+02	0.00E+00	0.00E+00
0.001	4.29E+01	2.53E+01	3.52E+01	4.06E+01	4.74E+01
0.01	3.03E+01	2.38E+01	2.63E+01	2.28E+01	3.35E+01
0.1	1.75E+01	1.57E+01	1.57E+01	1.38E+01	1.76E+01
1	7.09E+00	7.37E+00	6.65E+00	5.81E+00	8.30E+00
10	2.34E+00	2.96E+00	2.37E+00	2.47E+00	3.47E+00
100	4.58E-01	7.81E-01	5.01E-01	6.66E-01	1.07E+00
1000	9.58E-02	2.00E-01	1.40E-01	2.01E-01	3.06E-01
10000	7.50E-03	3.84E-02	1.04E-02	3.60E-02	7.60E-02
100000	0.00E+00	3.87E-03	2.72E-03	5.70E-03	2.57E-02

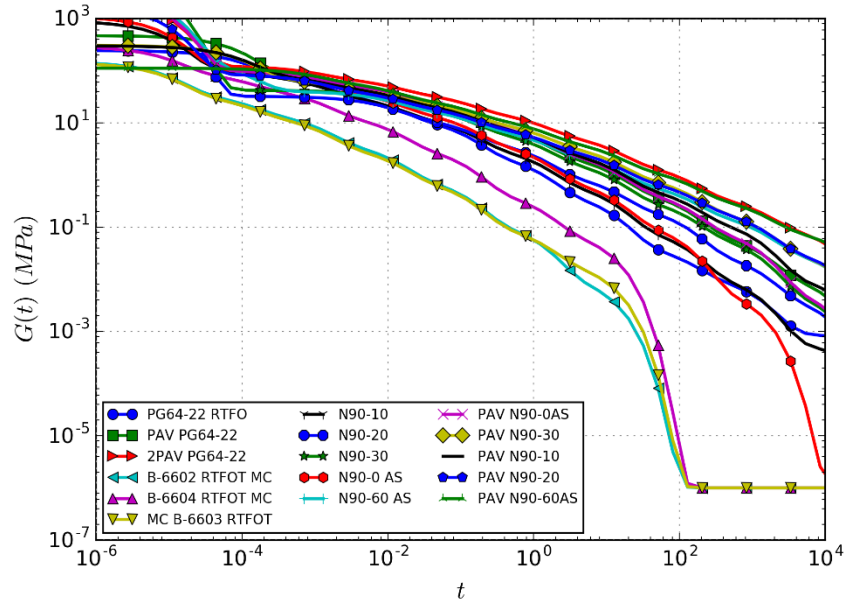


Figure 3-2 Relaxation shear modulus of studied binders.

3.2.3 Mortar

Mortar is defined as the combination of asphalt binder, air voids, and aggregates passing No. 8 (2.36 mm) sieve. The relationship between stress and strain was defined using linear viscoelasticity, and material constants were calculated using a micromechanical procedure (Li et al. 1999, Kim and Little 2004, Shu and Huang 2008a, and Shu and Huang 2008b). The procedure combines binder viscoelastic characteristics, aggregate gradation, and volumetric properties to determine the mortar relaxation modulus.

Based on micromechanical theories and energy considerations, it was found that the elastic modulus of a circular aggregate of radius a embedded in binder is:

$$E_o(a) = \frac{E_1(1 - n)(1 - v_o)}{x_1 - \frac{4E_2n}{E_1(1 - n)(1 - v_2) + E_2x_2}} \quad (3.2)$$

where: $x_1 = n(1 + v_1) + (1 - v_1)$,
 $x_2 = (1 + v_1) + n(1 - v_1)$,
 $n = (a/b)^2$,

E_1 and E_2 : elastic modulus of binder and aggregate, respectively,

v_1 and v_2 : Poisson's ratio of binder and aggregate, respectively,

$v_o = (v_2f_2E_1 + v_1f_1E_2)/(f_2E_1 + f_1E_2)$: Poisson's ratio of equivalent medium, and

f_1, f_2 , and f_3 : volume fraction of binder, aggregate, and air. f_3 was assumed to be constant and equal to 4%; $f_2 = 1 - VMA$ (VMA is obtained from the mix design); and

$f_1 = 1 - f_2 - f_3$

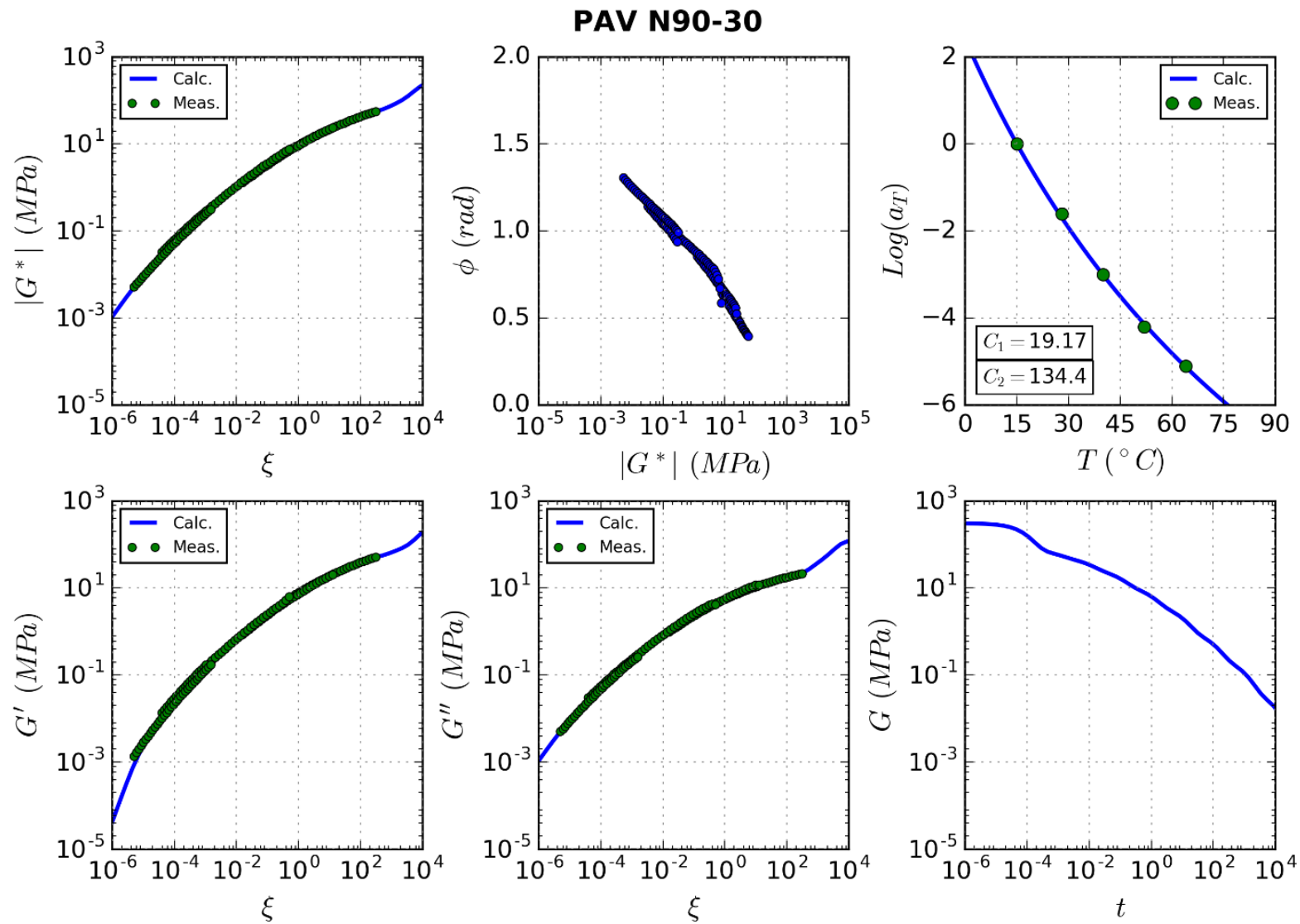


Figure 3-3 Dynamic shear modulus, phase angle, shift factor, storage shear modulus, loss shear modulus, and relaxation shear modulus for binder PAV N90-30.

Assuming the film of asphalt binder covering all aggregates had the same thickness:

$$b = a + \frac{f_1}{3f_2 \sum_{i=1}^{n-1} \frac{k_i}{r_i}} \quad (3.3)$$

where: r_i : average radius of the aggregate between the i th and $(i + 1)$ th sieve,
 n : number of sieves, and
 k_i : weight percentage of aggregate with size between r_i and r_{i+1} .

After the modulus for each aggregate radius is calculated, the modulus of the mortar is:

$$E_{mor} = \frac{1}{2} \sum_{i=1}^{N+1} [E_o(a_i) + E_o(a_{i+1})] k_i \quad (3.4)$$

where: $E_o(a_i)$ and $E_o(a_{i+1})$: elastic moduli for aggregate with particle size a_i and a_{i+1} , respectively.

If binder is no longer linear elastic but linear viscoelastic, correspondence principle can be used to find the mortar relaxation modulus. Hooke's law in Laplace domain is:

$$\bar{\sigma}(s) = \tilde{E}(s)\bar{\epsilon}(s) = s\bar{E}(s)\bar{\epsilon}(s) \quad (3.5)$$

where: s : Laplace variable,

$\bar{\sigma}(s)$ and $\bar{\epsilon}(s)$: Laplace transform of the stress and the strain,

$E(t) = E_e + \sum_{i=1}^n E_i e^{-t/\tau_i}$: relaxation modulus,

$\bar{E}(s)$: Laplace transform of the relaxation modulus, and

$\tilde{E}(s) = s\bar{E}(s)$: Carson transform

Consequently:

$$\tilde{E}(s) = s\bar{E}(s) = E_e + s \sum_{i=1}^m \frac{E_i \tau_i}{s\tau_i + 1} \quad (3.6)$$

Then, Eq. (3.2) in the Laplace domain becomes:

$$\bar{E}_o(s, a) = \frac{\tilde{E}(s)(1 - n)(1 - v_o)}{x_1 - \frac{4E_2 n}{\tilde{E}(s)(1 - n)(1 - v_2) + E_2 x_2}} \quad (3.7)$$

For the mortar:

$$\bar{E}_{mor}(s) = \frac{1}{2} \sum_{i=1}^{N+1} [E_o(s, a_i) + E_o(s, a_{i+1})] k_i \quad (3.8)$$

Relaxation modulus of the mortar can be recovered by taking inverse Laplace transform (Schapery 1962):

$$E_{mor}(t) = \bar{E}_{mor}(0.56/t) \quad (3.9)$$

The procedure to determine the relaxation modulus based on the gradation and the relaxation modulus of the binder is summarized in Figure 3-4. After mortar relaxation modulus was determined, the terms in the Prony series were calculated to be used as input in ABAQUS. Figure 3-5 presents a sample of the relaxation modulus of binder, the mortar relaxation modulus resulting from the binder and three different AC mixes, and the Prony series fit.

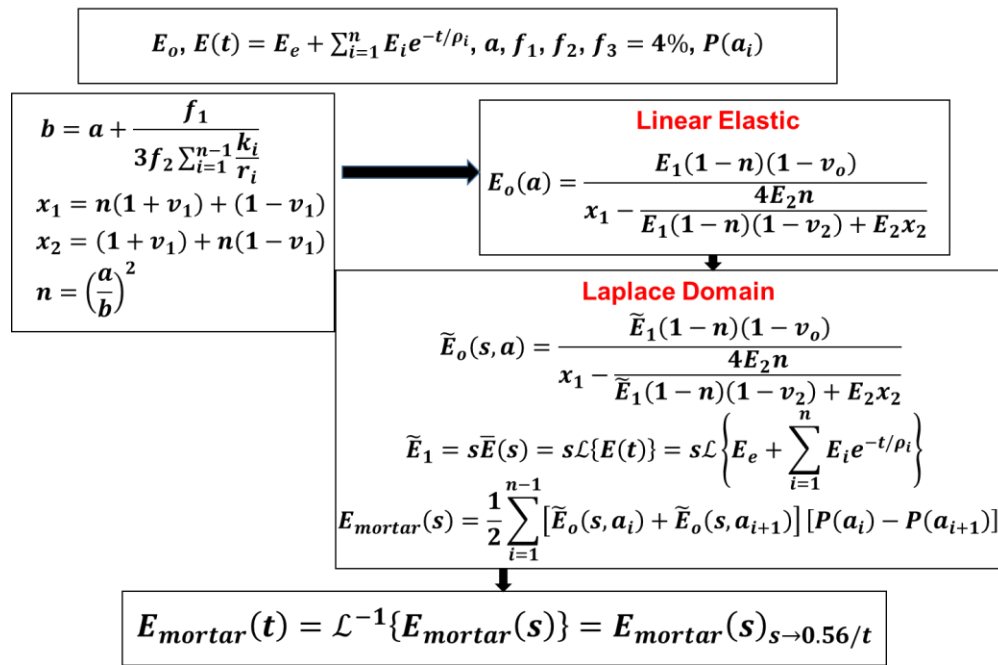


Figure 3-4 Determination of mortar relaxation modulus.

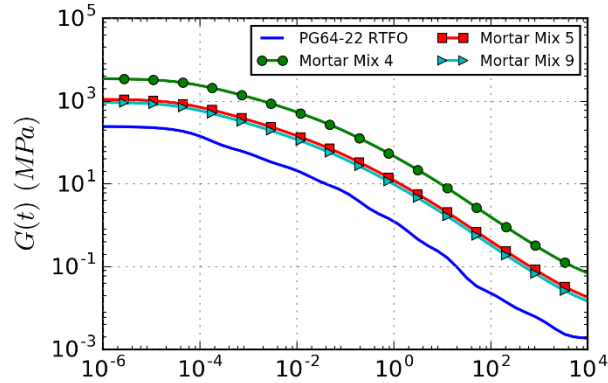


Figure 3-5 Relaxation modulus of binder, mortar, and Prony series fit for mortar relaxation modulus.

3.2.4 Mortar-Aggregate Interface

To determine the adhesion characteristics between binder and mastic, the tensile adhesion test was performed. The objective was to obtain load-displacement profiles when tensile forces are applied on the binder in contact with an aluminum substrate. Aluminum substrate and adhesion test setup was developed for sealants using the direct tensile test setup (Sawalha et al. 2017). Aluminum was chosen as substrate as a conservative choice to replace aggregates due to its low surface energy. The test fixtures made of aluminum and fabricated in-house were utilized to prepare binder samples as shown in Figure 3-6 and Figure 3-7. Notch lengths in these fixtures can vary according to the conditions of the test being conducted. The conditioning bath where samples were placed and tests were conducted can be used to maintain temperatures as low as -40 °C and as high as 25 °C in an alcohol medium.



Figure 3-6 Tensile adhesive method fixture in the bath before testing.



Figure 3-7 Tensile adhesive method fixture after failing.

A number of replicates were tested at different temperatures and loading rates to obtain visible adhesion failure on the surface of the substrate. Two different notch lengths (6 and 8 mm) and tests on unaged as well as short-term (RTFO) and long-term (PAV) aging were carried out. After numerous trials, a notch length of 6 mm for the binder PG 64-22 tested with aluminum and different aggregate types was selected. Extremely high and low temperatures can trigger cohesive failure in the binder or weak bonds at the interface, and, therefore, an intermediate temperature of -12°C was chosen to perform the test. For a different binder type, the selected temperature value would change accordingly, and a loading rate of 0.05 mm/sec was selected. Figure 3-8 presents a failed specimen, while Figure 3-9 shows a sample of the load-stroke curve. It can be inferred that a linear load–deflection curve persists until the maximum load is reached; the slope of the curve is 1100 N/mm approximately. This value was used as a reference for spring coefficient between aggregates and mortar



Figure 3-8 Failed specimen.

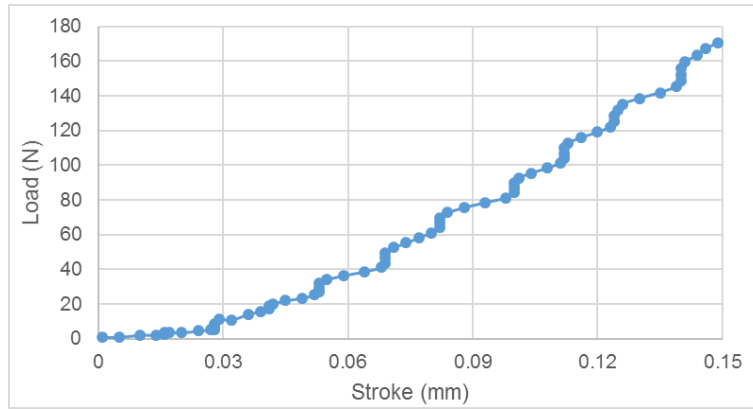


Figure 3-9 Sample of adhesion test between binder and aggregate.

3.3 CONTINUUM FRACTURE TEST MODEL

The continuum model has the potential of providing a bridge between continuum pavement model and I-FIT results. The bridge may rely on the correspondence principle and equivalent materials. The correspondence principle can capture the viscoelasticity of the mortar on the micromechanical model and find an equivalent elastic modulus in the continuum I-FIT model. At the same time, a relationship between the continuum pavement and I-FIT model can be explored.

ABAQUS was used to predict the global load-displacement curve, strain field in the x direction around the notch, and J -integral. The 2-D I-FIT model, shown in Figure 3-10, had a diameter of 150 mm, and a 15 mm long by 1.5 mm wide notch sawed at the sample's center. Once placed in the loading frame, the monotonic load was applied on the upper part of the sample. Two supports were located 60 mm away from the center of the specimen. Loading frame and supports were modeled as analytical rigid surfaces, while displacements along the x and y direction, as well as rotation with respect to the z axis of the supports' reference nodes were constrained. On one hand, the interaction between supports and specimen was assumed frictionless, as specified by the AASHTO standard. On the other hand, slipping between loading frame and specimen was prevented to avoid rigid body motion instability.

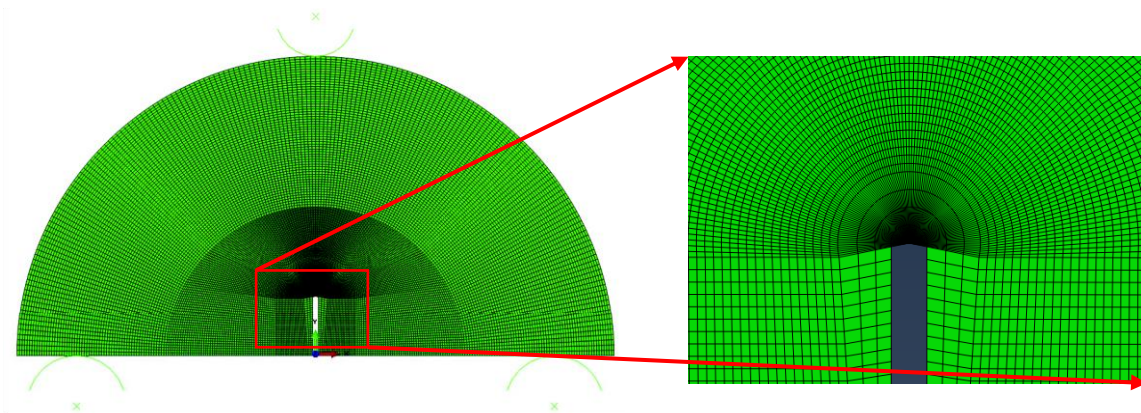


Figure 3-10 Linear elastic homogeneous I-FIT model.

The model was meshed with 24064 four-node continuum plane-strain bi-linear FEs. In this case, the material was assumed linear elastic with modulus of 260 MPa and a Poisson's ratio of 0.3. These values were set after a calibration process using digital image correlation (DIC) measurements as reference.

3.4 MICROMECHANICAL FRACTURE TEST MODEL

Geometry, loading, boundary conditions, and contact properties for the micromechanical model were equivalent to the linear elastic continuum case described in the previous section. However, the material was not assumed linear elastic homogenous isotropic; but consisted of aggregate and mortar. Aggregate and mortar were considered linear elastic and linear viscoelastic, respectively, while the aggregate–mortar interface was defined by nonlinear springs along the x and y direction. The springs had different load–deflection behavior in tension and compression. In tension, the spring was linear elastic up to an opening value where the tension force was kept constant. In compression, the spring constant was high enough to prevent penetration from the aggregate to the mortar and vice versa. More details regarding this approach were presented by Ghauch et al. (2015).

Two approaches were developed to define the aggregate distribution in the I-FIT sample. The first one is based on images obtained from actual I-FIT specimens before testing. The pictures were processed using the software Simpleware, which can differentiate between various phases in an image. The second approach is based on a Python script that combines aggregate gradation, volume in mineral aggregates (*VMA*), and Voronoi tessellations to create a random aggregate distribution that satisfies the mixture volumetric properties. More details regarding the implementation and use of both models are discussed in the following chapter.

CHAPTER 4 - MODEL CALIBRATION AND VALIDATION

FE model of both, continuum and micromechanical representation, were calibrated and validated using laboratory measurements. For the continuum model, low-density polyethylene (LDPE) was tested using the I-FIT protocol. Strain fields were measured using DIC and compared with results from the FE model. Good agreement guarantees appropriate numerical representation of the I-FIT. For the micromechanical model, DIC was used to measured strain fields, and representation of aggregates and mortar distribution demanded the use of a specialized software, Simpleware. This chapter not only details the validation and calibration process, but also describes DIC technology and Simpleware implementation.

4.1 DIGITAL IMAGE CORRELATION

DIC is a non-contact full-field measuring technique with multiple applications in experimental mechanics. This method is based on the acquisition of successive images of a speckle pattern applied over the surface of a body before a traction force is applied. As a result, the body is subjected to a stress field and pictures were taken during the stressed condition and compared to a reference image taken before applying the traction (Sutton et al. 2009). The comparison allows the measurement of displacements, strains, and stresses (the latter through appropriate constitutive equations) on the entire surface of a specimen for the time corresponding to each picture taken (Sutton et al. 2009). DIC has been used to study fracture properties of composites (Leclerc et al. 2009), metals (Carroll et al. 2013), functionally graded materials (Abanto-Bueno and Lambros 2002), concrete (Wu et al. 2011, Skarżyński et al. 2013), and asphalt (Wu et al. 2011).

In this study, DIC was used to measure the displacement and strain fields within the I-FIT microstructure. A random speckle pattern was applied on the surface where the DIC measurements were taken using an air brush. Then, a high-resolution, charge-coupled device camera captured successive images of the specimen during the test. An Allied Vision Prosilica GX6600 camera was used at a rate of four frames per second and a resolution of 6576 x 4384 pixels. Then, subsets of pixels were compared with a deformed picture (taken at a loaded state) to find a best match and thus compute the deformation of the subset (i.e., the displacement and the displacement gradients corresponding to the center of the subset). The reference image was captured when a contact load of 0.1 kN was applied to the specimen to reduce the rigid body motion during the experiment.

DIC assumes that the deformation of each subset is homogeneous in-plane and that the specimen surface speckle pattern light intensity remains unchanged throughout deformation, which implies light uniformity as well as the absence of speckle deterioration. The light uniformity was achieved using two white laps so that each point on the specimen maintains the same recorded grayscale value throughout the experiment, thus allowing correlation with the reference picture. With these assumptions, the deformation at a point was computed using the procedure outlined by Chu et al. and Bruck et al. (Chu et al. 1985, Bruck et al. 1989). A commercial software Vic2D was used for the correlation analysis. With these assumptions, the equations governing the deformation at a point are as follows:

$$x' = x + u + \frac{\partial u}{\partial x} \Delta x + \frac{\partial u}{\partial y} \Delta y, \quad (4-1)$$

$$y' = y + v + \frac{\partial v}{\partial x} \Delta x + \frac{\partial v}{\partial y} \Delta y, \quad (4-2)$$

where x and y are Cartesian position coordinates, u and v are the corresponding displacements, and prime (') denotes the variables in the deformed frame.

4.2 CALIBRATION OF THE CONTINUUM I-FIT FE MODEL

The linear elastic I-FIT FE model was validated by comparing the global load–deflection curve and the strain field in the x direction ε_{xx} with measurements from the testing machine and the DIC, respectively. A sample made of LDPE was subjected to the I-FIT (see Figure 4-1). The testing machine applied the load at a rate of 50 mm/min and measured the resulting force. In addition, DIC was utilized to measure the displacement/strain field every 0.5 sec. Information up to 7 sec was used for validation purposes, corresponding to a displacement of 5.63 mm and a load of 12.9 kN. It is worth mentioning that the specimen failed at a load of 20.4 kN and displacement of 12.67 mm.



Figure 4-1 LDPE sample under I-FIT.

The measured and calculated load–deflection curves are compared in Figure 4-2. The figure also shows the mean average percentage error $MAPE$, root-mean square error $RSME$, coefficient of determination R^2 between the measured and calculated deflection. Overall, the I-FIT FE model results demonstrate the capability of numerical model simulate actual load–displacement curve with reasonable accuracy when an appropriate modulus of the specimen was selected. The agreement between both curves decreased as the applied load became higher. There are two possible explanations for this behavior. First, the LDPE is assumed linear elastic, and the load–

deflection curve clearly shows some degree of nonlinearity, which becomes more pronounced as the load increased. Second, some portion of the measured displacement can be attributed to machine compliance. Previous studies have suggested that in the case of the I-FIT machine, displacements created by machine compliance can be in the order of 0.1 to 1 mm depending on the loading frame and fixtures (Barber 2016).

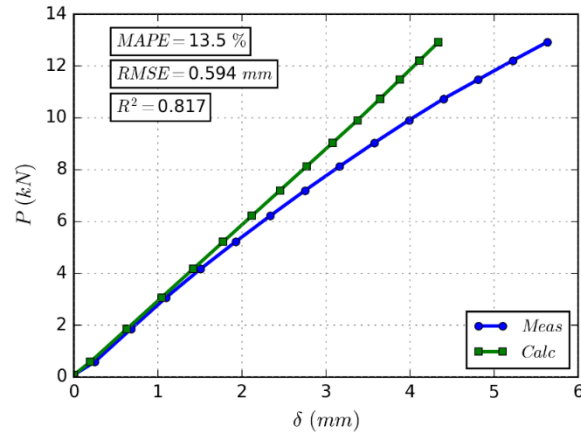


Figure 4-2 Global load–displacement curve for LDPE specimen.

A more relevant comparison from the point of view of fracture properties was performed using DIC. Strains in the opening direction were contrasted at every time increment for the region around the notch where $-30 \text{ mm} < x < 30 \text{ mm}$ and $10 \text{ mm} < y < 45 \text{ mm}$ with the origin taken at the center of the notch (see Figure 3-10). Figure 4-3 shows the comparison for the last time increment before the peak load is reached, which represents a load of 12.91 kN. The horizontal axis corresponds to horizontal strain from the FE model and the vertical axis to DIC measurements. The plot also presents $RMSE$ and R^2 . $RMSE$ and R^2 were found to increase as the applied load increased. After the load reached 8.12 kN, $RMSE$ and R^2 varied between 1580 and 1830 $\mu\epsilon$ and 0.67 and 0.93, respectively. Good agreement between measurements and calculation indicates a good representation of the I-FIT in the FE model.

Once there is a good match between the model and the experimental measurements, fracture variables such as stress intensity factor (SIF) and J -integral can be studied. The SIF for a cracked (not notched) SCB with a ratio between support span and radius of 0.8 is given by (Lim et al. 1993):

$$K_{I,cr} = \frac{P}{2rt} \sqrt{\pi a} Y_I = \frac{P}{2rt} \sqrt{\pi a} \left[4.782 - 1.219 \frac{a}{r} + 0.063 \exp\left(7.045 \frac{a}{r}\right) \right] \quad (4-3)$$

where: $K_{I,cr}$: SIF for cracked SCB

P : applied load

r : specimen radius

t : specimen thickness

a : notch length

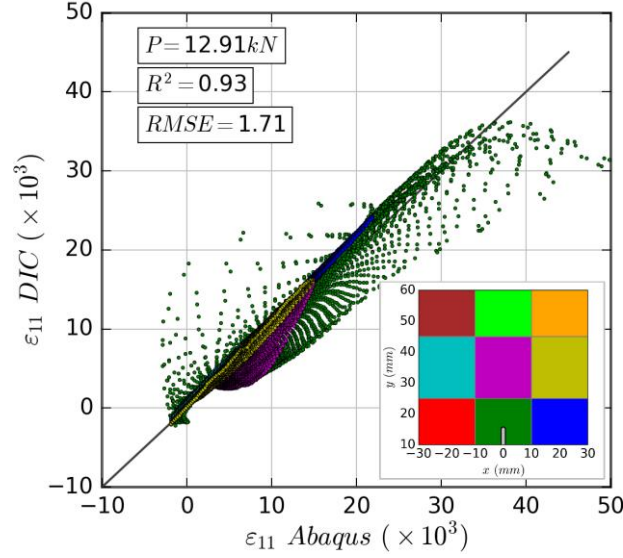


Figure 4-3 Comparison of ε_{11} between DIC measurements and ABAQUS results.

For the case of $a=15$ mm, $r=75$ mm, and $t=50$ mm, $Y_I=4.80$:

$$K_{I,cr} = 2.400 \frac{P}{rt} \sqrt{\pi a} \quad (4-4)$$

However, the actual SCB specimen is not cracked but notched, and, consequently, Eqs. (4-3) and (4-4) might not be accurate. In order to obtain a formula for the SIF of a notched SCB, the J -integral was calculated using ABAQUS for a wide range of applied loads ($0.5 \text{ kN} < P < 5.0 \text{ kN}$) and elastic moduli ($100.0 \text{ MPa} < E < 50000 \text{ MPa}$). The following expression for the J -integral was found:

$$J_{nt} = 11.655 \frac{P^2 a}{E^* t^2 r^2} \quad (4-5)$$

where: $E^* = E/(1 - \nu^2)$
 E : elastic modulus
 ν : Poisson's ratio

Considering the relationship between J -integral and SIF for linear elastic materials ($J = K_I^2/E^*$), it can be found that the SIF for a notched SCB, $K_{I,nt}$, is:

$$K_{I,nt} = 1.926 \frac{P}{rt} \sqrt{\pi a} \quad (4-6)$$

Therefore, comparing Eqs. (4-4) and (4-6):

$$K_{I,nt} = 0.803 K_{I,cr} \quad (4-7)$$

4.3 VALIDATION OF MICROMECHANICAL FE MODEL

Comparison between DIC measurements and FE model predictions in the micromechanical model required the determination of aggregate distribution in the I-FIT sample. The position of the aggregates was defined by analyzing and processing images using the software Simpleware. Simpleware was used to visualize, analyze, quantify and process images and generate input files for FE analysis. The process of obtaining the input file for FE analysis can be divided into two steps. The first one is the image processing itself, and the second one is the thresholding and segmentation.

4.3.1 Image Processing

Images captured on gyratory-compacted samples using a digital camera were processed to correct the white balance and color profile. For this purpose, the image processing softwares GIMP were utilized, so the images were suitable for manipulation in Simpleware. Figure 4-4 summarizes the process applied to images from the digital camera. A second source of images were obtained from a synthetic microstructure generator using the Python script presented in section 5.1. These computer-generated images did not require any preprocessing using GIMP before being manipulated in Simpleware.

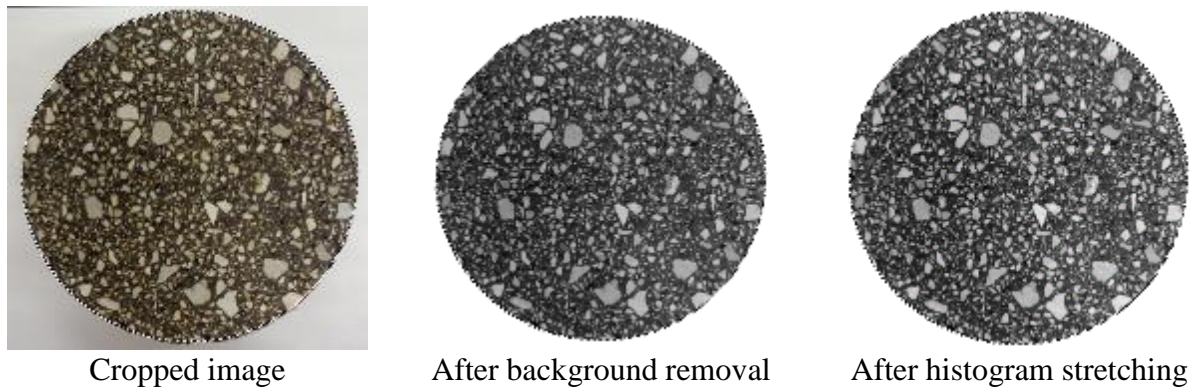


Figure 4-4 Processing of images taken from a digital camera.

4.3.2 Image Thresholding and Segmentation

Images were imported in Simpleware and then filtered and segmented with respect to the thresholds defined for each phase in the 3-D sample (2-D images were converted to a 3-D sample via replication). In an AC sample, three major phases are usually considered for observation: aggregates, mastic (asphalt with fines), voids (see Figure 4-5). For this study, two phases were included (aggregate and mortar) and voids were assumed in the mortar phase. Figure 4-6 shows a usual functioning window in Simpleware depicting how the grayscale intensities (ranging from 0 to 255) can be assigned to the aggregate or mastic phases depending on the density of the material in each phase. The high end of the grayscale is generally attributed to aggregates and vice versa for the mastic phase. Typically, air voids belong to the lowest range of the grayscale.

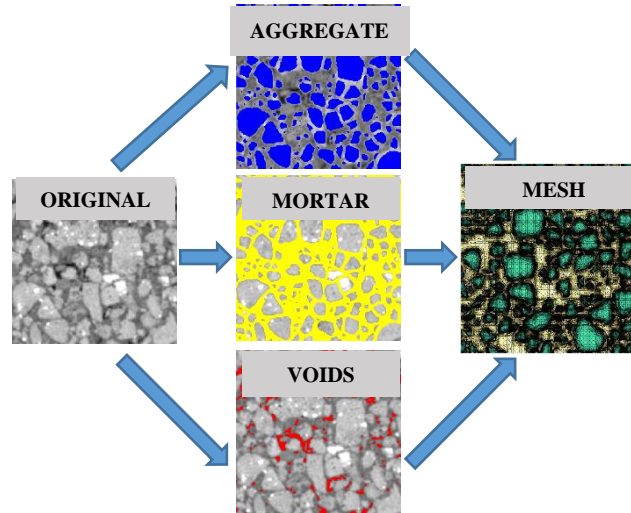


Figure 4-5 Different phases defined in the Simpleware image segmentation (Ghauch et al. 2015).

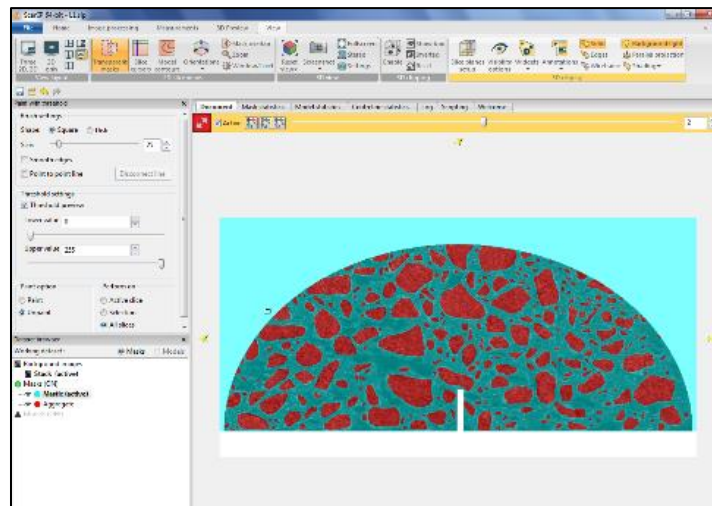


Figure 4-6 Typical functioning window in Simpleware.

As seen in Figure 4-6, no contact is considered between aggregates, which represents a basic premise for the current analysis. Therefore, the two major phases were defined such that all aggregates are disconnected at a feasible distance from each other (aggregates that are closely spaced or in contact can make mesh generation procedure very expensive), and contact algorithms between aggregates can be computationally prohibitive. Smoothing algorithms along with other functions for a clear segregation of the different phases were also used. A mesh was generated in the next step by defining the values of parameters which described the degree of fineness or coarseness of the mesh. A series of hit and trials was performed to get the best optimal values of these parameters. Triangular FE elements were selected for this study to facilitate a simple mesh fine enough to capture all the critical responses generated in the analysis stage. After the mesh was generated using Simpleware, it was exported to the ABAQUS analysis software. Figure 4-7 shows a sample of very fine mesh.

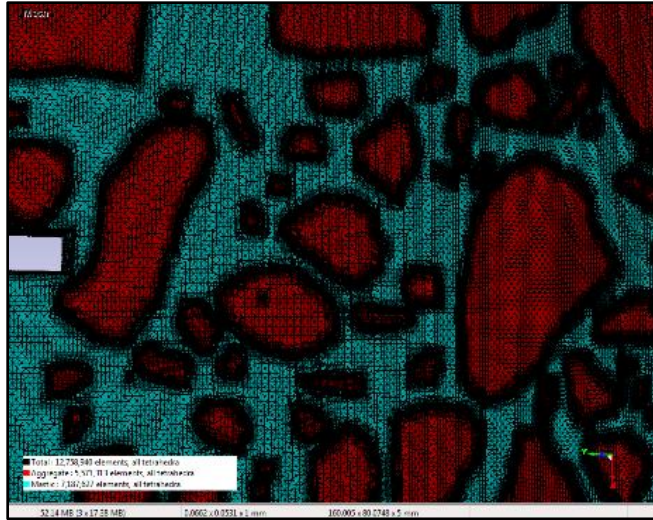


Figure 4-7 Mesh generated in Simpleware.

4.3.3 Comparison between Measured and Calculated Strains

A Python script was written to fine-tune Simpleware’s output. The script converted the three-dimensional mesh from Simpleware into a two-dimensional model. In addition, it assigned material properties, loading, and springs at the interface between aggregate and mortar. A preliminary sensitivity analysis and adhesion test proved that spring constants of $k_x=k_y= 1000$ N/mm and aggregate elastic modulus of 60 GPa was appropriate to study the I-FIT responses.

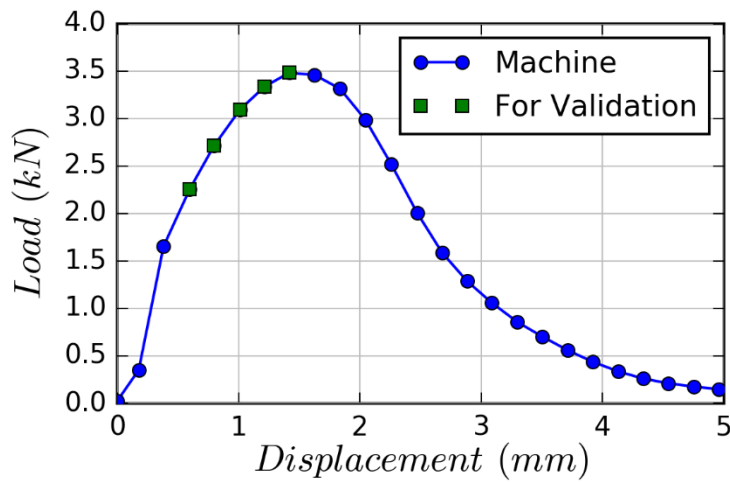


Figure 4-8 I-FIT load–displacement curve used for validation.

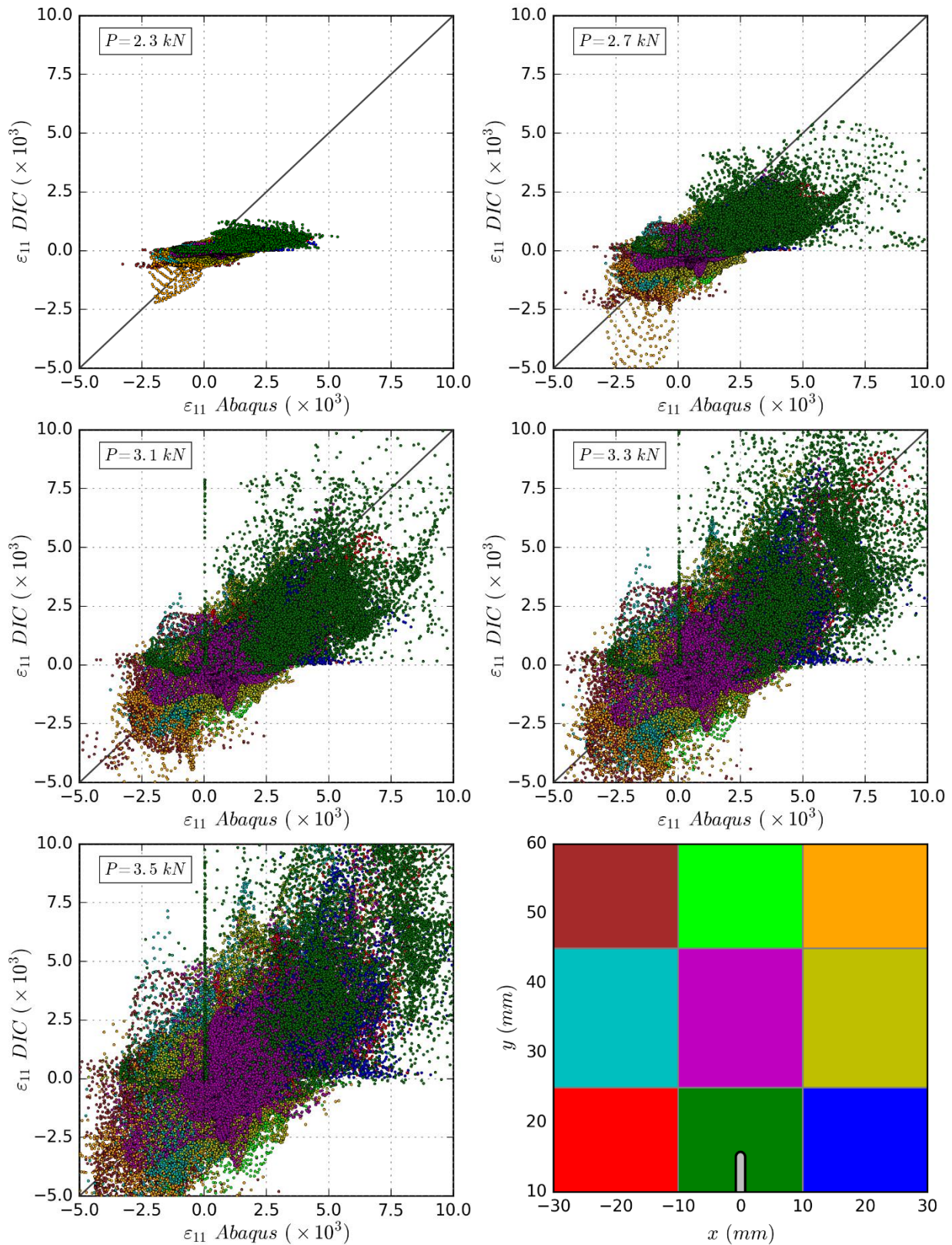


Figure 4-9 Comparison between measured and calculated opening strains in micromechanical model at carious loadings.

Validation was performed by comparing measured and calculated strain fields. The measurements were obtained using DIC during I-FIT, and the load–displacement curve is shown in Figure 4-8. The dots in the curve represent points where DIC images were captured, but only strains for loads of 2.2, 2.7, 3.1, 3.3, and 3.5 kN were compared with calculations from the FE model. To create the FE model, not only the elastic modulus and aggregate–mortar interface, but also mortar properties using the procedure in section 3.2.3 were used. Figure 4-9 compares the measured and calculated opening strains for various loads. The colors in the subfigure correspond to a location in the I-FIT sample as shown in the bottom-left plot. Since a threshold of $20 \mu\epsilon$ was set for a measurement to be compared, the amount of points in each subfigure changes. The amount of points in the cloud increased with the load, and it was 78967 and 83876 points for a load of 2.3 and 3.5 kN, respectively. The match between measurement and calculation is acceptable considering there is no calibration in the input parameters. It can also be observed that the general agreement increased with load, and that there is more dispersion in the cloud of points as load increased.

CHAPTER 5 - EVALUATION OF MICROSTRUCTURAL FACTORS AFFECTING FRACTURE OF ASPHALT MIXES

A parametric study was performed to determine the effect of aggregate structure, binder, and mortar–aggregate interaction on the fracture characteristics of AC based on numerical modeling of the I-FIT. Synthetic images of various mixes were generated and modeled in I-FIT. The objective of these models was to develop a relationship between microstructural features and cracking resistance or potential of I-FIT that can be used in large scale pavement modeling. Nine AC mix designs were considered, and ten I-FIT replicates were generated using the Python script described below. The mortar properties were obtained using the gradation of each mix and binder relaxation modulus as described in Section 3.2.3. Three binders covering the stiffness spectrum were included in the sensitivity analysis.

5.1 COMPUTER-GENERATED FRACTURE TEST SPECIMENS

A Python algorithm was developed to create artificial I-FIT samples. Using sieve analysis, VMA, and geometric details of the I-FIT sample as input parameters, the amount of aggregates and corresponding area in each sieve could be calculated. Then, a random cloud of points was generated to create Voronoi tessellations, which would form potential aggregates for each sieve size in the final artificial gradation. A sample of the Voronoi tessellations is presented in Figure 5-1. The dots inside the polygons are input; the lines determining the polygons are perpendicular to the midpoint of the line connecting two dots. The resulting polygons are candidates and will be part of the I-FIT sample as long as they satisfy size and shape requirements.

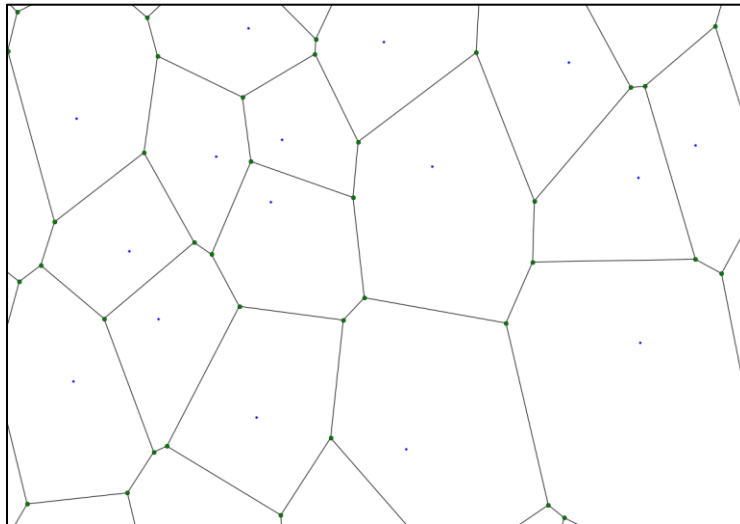


Figure 5-1. Sample of Voronoi tessellations.

A series of requirements was applied to the potential aggregates before they were selected for the final gradation. First, the area was inside a specified tolerance of 5% the area of a circle with the same diameter as the corresponding sieve size. In addition, individual aggregates were restrained

to have more than three sides (i.e., no triangular aggregates were allowed). Using the maximum and minimum distance in the aggregate, two additional criteria were checked: i) the minimum distance had to be less than the sieve opening, and ii) the ratio between the maximum and minimum distance in the aggregate was less than five to limit the use of flat and elongated particles.

After the final aggregates were selected from the candidates in the Voronoi tessellations, the particles were placed inside the I-FIT geometry. The process was performed one particle at a time, starting from the coarsest aggregate. The particle centroid was assigned a polar coordinate with respect to the center of the I-FIT, and the coordinate was randomly changed until the aggregate did not intersect any other particle. Figure 5-2 presents a sample of the computer-generated I-FIT specimen.

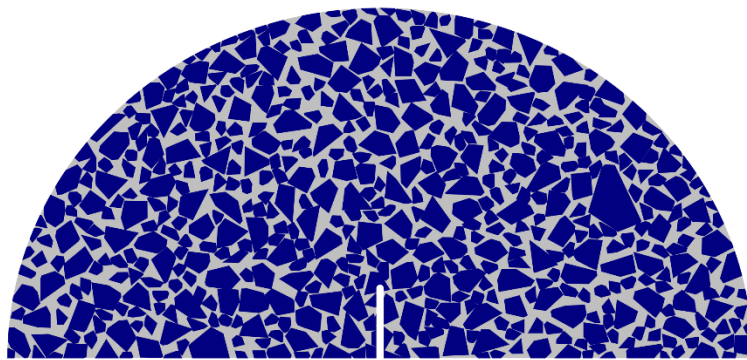


Figure 5-2 Sample of computer-generated I-FIT specimen.

Nine aggregate structures of AC mixes designed in the laboratory were selected to study the fracture behavior using the I-FIT. A wide range of aggregate gradations with varying voids in mineral aggregates (VMA), nominal maximum aggregate size (NMAS), and gradation types (dense coarse, dense fine or gap-graded) were chosen to evaluate the impact of microstructural variation on the modeling results. Some of these mixes are not commonly used in overlays; however, they contributed to the development of a database of images and results to understand the influence of key microstructural features on fracture resistance. The VMA of the gradations varied between 13.8 and 19.2 %, and the sieve analysis showed the aggregate structures located above and below the maximum density line. Figure 5-3 and Table 5-1 show the sieve analysis for the selected aggregate structures. Table 5-1 also presents the original designation of each AC mix along with its label in the current study and *VMA*.

N50 and 163M(L)-N08 correspond to leveling AC mixes with high VMA and high binder content, while 157M-Y03 and L3 are surface mixes with 12.5-mm NMAS. D5 Control refers to a control mix in the study aimed at examining the effect of high RAP content on AC performance of AC mixes in Illinois (Al-Qadi et al. 2012). The other four AC mixes were initially designed for the study of overlays: F-mix is a dense-graded AC used as surface mixture in Illinois; 12.5 mm stone mastic asphalt (SMA) is one of the control mixes in the study; Slag/Fiber mix is a fine-graded fiber-reinforced steel slag mix; and 4.75 mm SMA has a NMAS of 4.75 mm, which allows overlays thickness as low as 19 mm (Al-Qadi et al. 2013). SMA is a gap-graded mix that

relies on aggregate contact to better perform under rutting, leaving more space for binder and fine aggregate (i.e., mortar).

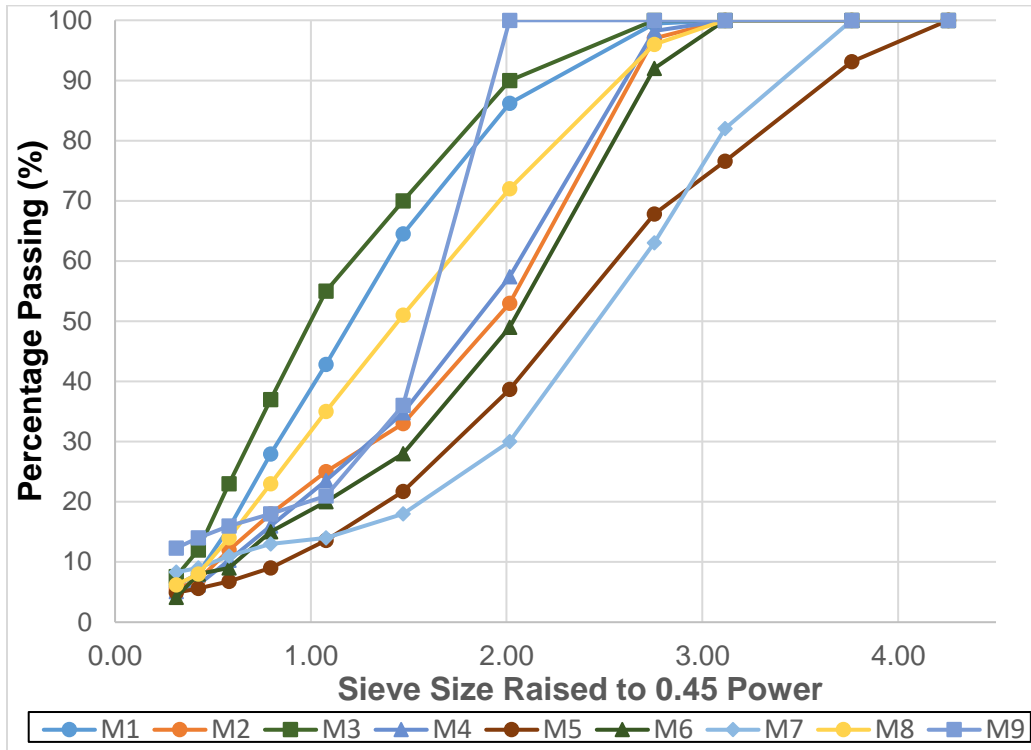


Figure 5-3 Gradation of selected aggregate structures.

Ten replicates of each gradation were created using the Python script considering two phases: aggregate and mortar (i.e., a combination of asphalt binder, air, and aggregates passing No. 8 sieve). A sample from the output of the Python script for the nine mixes showing the two phases is presented in Figure 5-4. In addition, Figure 5-5 presents the variation of *VMA*, mean ratio between areas of mortar and I-FIT sample in percentage for the nine AC mixes, and the mortar ratio calculated from the mix design information. The mortar ratio also includes error bars, which were calculated as the ratio between the standard deviation and the square root of the number of sample in the case of *VMA*. The error bars represent the variability of the values between the various replicates (error is too small to be noticed in the plot). A similar trend for the variations is observed except for Mix 7 (12.5-mm SMA) and Mix 9 (4.75-mm SMA), where even though the *VMA* increased with respect to the precedent mix (Mix 6 and Mix 8, respectively), the mortar ratio decreased. This may be due to the difference in the gradation type.

Table 5-1 Gradation, Binder Content, and VMA of Selected Aggregate Structures

Sieve	N50	157M-Y03	163M(L)-N08	L3	D5 Control	F-Mix	12.5 mm SMA	Slag/Fiber Mix	4.75 mm SMA
	Mix 1	Mix 2	Mix 3	Mix 4	Mix 5	Mix 6	Mix 7	Mix 8	Mix 9
1" (25.0 mm)	100	100	100	100	100.0	100	100	100	100
3/4" (19.0 mm)	100	100	100	100	93.1	100	100	100	100
1/2" (12.5 mm)	100	100	100	100	76.6	100	82	100	100
3/8" (9.5 mm)	99	97	100	98.2	67.8	92	63	96	100
No. 4 (4.75 mm)	86	53	90	57.4	38.7	49	30	72	100
No. 8 (2.36 mm)	65	33	70	34.8	21.7	28	18	51	36
No. 16 (1.18 mm)	43	25	55	23.5	13.6	20	14	35	21
No. 30 (600 µm)	28	18	37	16	9.0	15	13	23	18
No. 50 (300 µm)	16	12	23	10.3	6.8	9	11	14	16
No. 100 (150 µm)	8	7	12	6.2	5.6	8	9	8	14
No. 200 (75 µm)	6	5.5	7.6	5.1	4.9	4.1	8.3	6.2	12.3
VMA	18.4	15.0	19.2	15.3	13.8	14.5	17.6	15.4	18.5
Binder Type	PG 70-22	PG 58-28	PG 70-28	PG 64-22	PG 64-22	PG 70-22	PG 76-22	PG 70-22	PG 70-22
Binder Content (%)	7.5	5.8	8.0	6.0	5.2	5.1	6.0	5.7	7.3
Air Voids in Model (%)	4.0	4.0	4.0	4.0	4.0	4.0	4.0	4.0	4.0

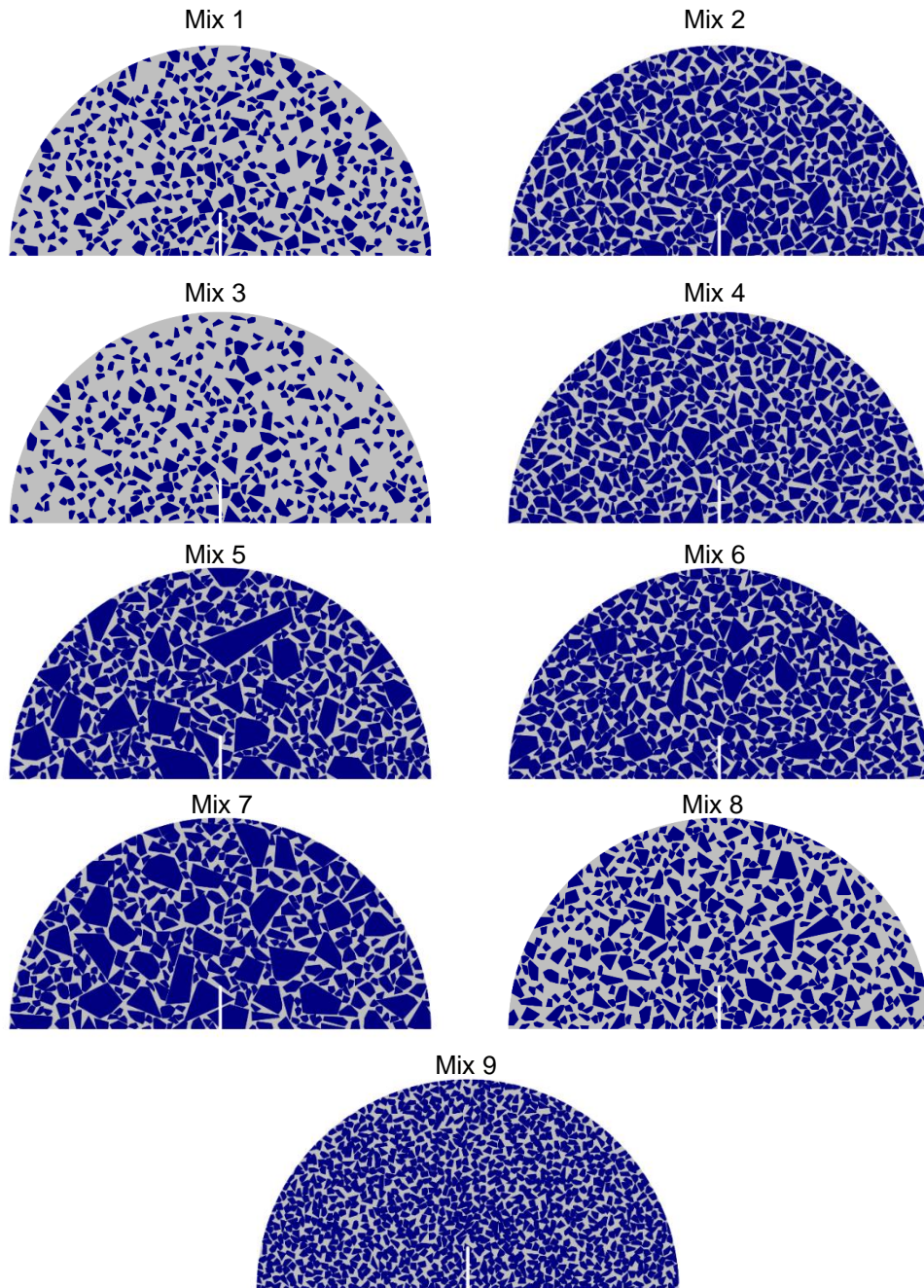


Figure 5-4 Sample of resulting images from Python script for each mix.

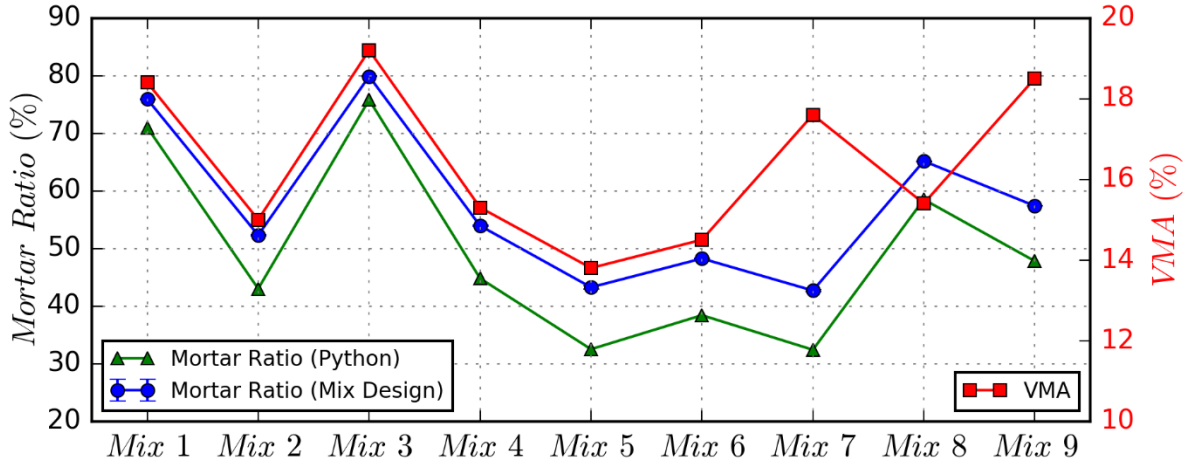


Figure 5-5 Mortar ratio and VMA for the nine mixes.

5.2 FRACTURE RESPONSE TO LOADING

Fracture response to loading of specimens was assessed using various criteria. First, the variation of opening stress and strain (σ_{11} and ε_{11} , respectively) was plotted along four paths. Paths 1, 2, and 3 extended along the x axis from $x=-30$ mm to $x=30$ mm at three distances from the bottom of the specimen ($y=0$ mm). For Path 1, $y=20$ mm; for Path 2, $y=25$ mm, and for Path 3, $y=35$ mm. On the other hand, the fourth path extended along the vertical direction at a horizontal location coinciding with the notch ($x=0$ mm) from $y=20$ mm to $y=65$ mm. The locations of the paths are presented in Figure 5-6.

In addition to the stresses and strains in the opening direction along Paths 1-4, an energy term of the elements inside the hatched area Figure 5-6 was calculated. The area was defined by all the points inside a circumference of diameter 35 mm with center at $x=0$ and $y=32.5$ mm and outside a circumference with center at $x=0$ and $y=17.5$ mm with diameter of 5 mm. Points inside the smaller circumference were discarded because this zone might experience deformation levels outside the linear limits, and the mesh is not fine enough to capture high stress gradient caused by the singularity. The energy term was calculated as:

$$Energy = \sum_{i=1}^e A_i \times (\varepsilon_{11}\sigma_{11} + \varepsilon_{22}\sigma_{22} + \varepsilon_{12}\sigma_{12}) \quad (5.1)$$

where e : total number of elements in the hatched area,

A_i : area of element i , and

ε_{kl} and σ_{kl} : strain and stress along direction k on face l , respectively.

Finally, the load applied during the displacement-controlled test was also extracted from the FE analysis.

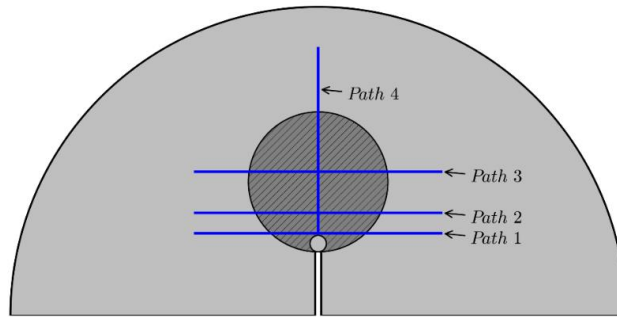


Figure 5-6 Location of paths for variation of σ_{11} and ϵ_{11} .

5.2.1 Gradation Effect

To determine the effect of aggregate gradation on the fracture behavior, ten replicates of the nine mixes in Figure 5-3 with mortar properties defined by binder PG 64-22 RTFO were modeled. It should be noted that having the same binder does not translate into having the same mortar because of differences in gradation. For this analysis, the aggregate–mortar interface was fixed at $k_x=k_y= 1000$ N/mm. As previously explained, the mortar viscoelastic characterization was found using binder relaxation modulus and mixture gradation (see section 3.2.3).

Figure 5-7 presents the shear relaxation shear modulus $G(t)$ for the binder PG 64-22 PAV and the resulting mortar for each of the nine mixes presented in Figure 5-3 and Table 5-1. It should be noted that mortar modulus depends on the aggregate gradation and VMA , and it is independent from aggregate particle distribution in the test specimen. Consequently, the mortar relaxation modulus is same for the ten replicates in each mix. The matching curves in Figure 5-7 do not imply the same mechanical responses because the gradation of each mix is different, which will affect the micromechanical response as they represent aggregate phase.

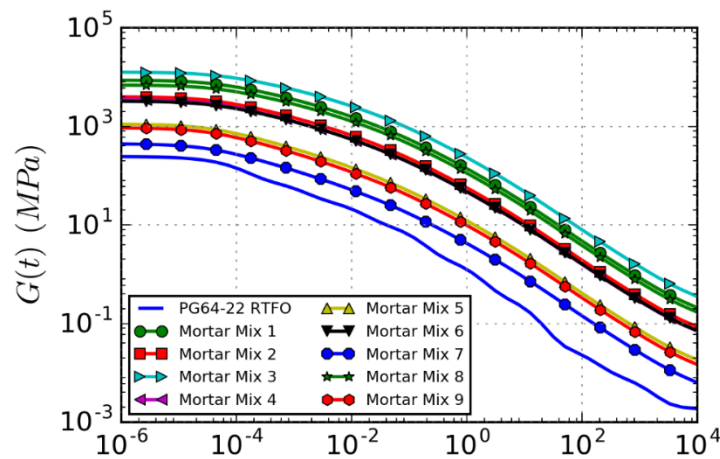


Figure 5-7 Shear relaxation modulus for binder PG 64-22 RTFO and resulting mortars in Mixes 1 through 9 (reference temperature: 15 °C).

The ranking of the mortar stiffness can be explained considering *VMA*, mortar ratio, and the percentage passing No. 16 sieve (P_{16}). The mix with the lowest mortar ratio, Mix 7, resulted in a mortar with the lowest $G(t)$. The shear relaxation modulus of mortar of Mix 5 was slightly higher than mortar of Mix 9 even though their gradation curves were considerably different. Based solely on higher P_{16} , the mortar of Mix 9 was expected to have higher $G(t)$; however, Mix 9 contained higher binder content thus reducing $G(t)$ of the resulting mortar. It should be noted that all of these mixes contained the same binder type. In reality, SMA's and AC mixes used in thin overlays would use a polymer-modified binder that can result in higher mortar stiffness values.

The mortar in Mixes 2, 4, and 6 also had similar shear relaxation modulus, and the similarities were caused by similar values of P_{16} and *VMA*. Mix 8 and Mix 1 provided higher shear relaxation modulus than Mixes 2, 4, and 6 due to their higher P_{16} , and $G(t)$ for the mortar in Mix 8 was lower than in Mix 1 because of the lower P_{16} and *VMA*. The stiffest mortar was observed in Mix 3 because of its highest P_{16} , *VMA*, and mortar ratio. A summary of the ranking is illustrated in Figure 5-8 for the relaxation shear modulus evaluated at $t=1$, $G(1.0)$ along with P_{16} .

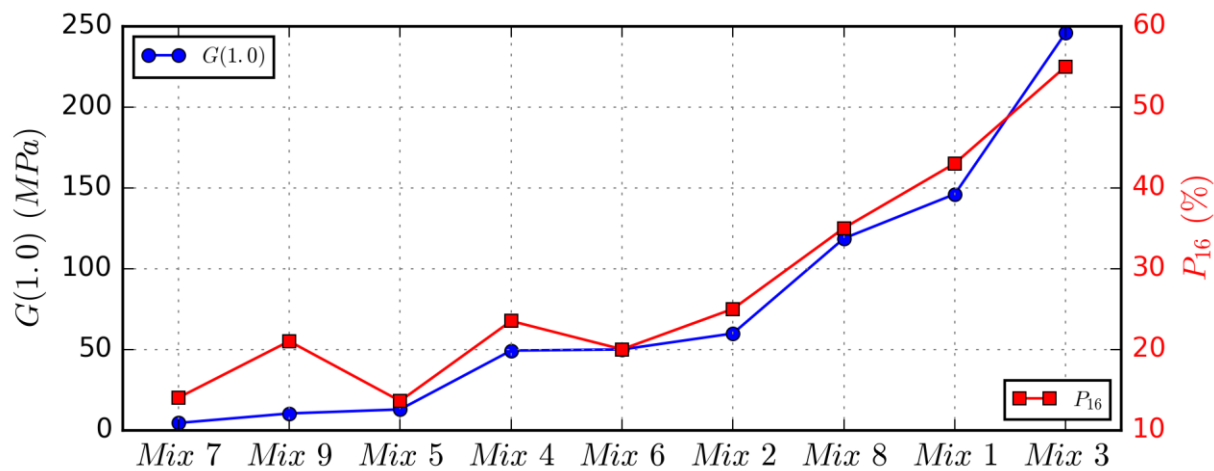


Figure 5-8 Shear relaxation modulus at $t=1.0$ s and P_{16} for studied mixes.

Applied Load

Figure 5-9 presents the mean force and its variations due to the number of replicates generated for Mixes 1 through 9 applied by the loading head. The figure also presents relaxation shear modulus of the mortar at $t=1.0$ s. The values are shown in ascending order, and the same trend is observed for both variables indicating a high correlation between mortar modulus and applied load. In addition, the error of ten replicates was very low, with Mix 6 having the highest error (0.0498 kN).

The information presented in Figure 5-9 indicates the effect of coarse aggregate on the applied load. Mortars of Mix 6 and Mix 4 have similar shear relaxation modulus, but the applied load for Mix 6 (1.51 kN) is 16% higher than for Mix 4 (1.29 kN). As seen in Figure 5-3, the aggregate

gradation of Mix 6 is coarser than of Mix 4, thus increasing the overall stiffness of the I-FIT sample and, consequently, the applied force. A similar behavior was observed for Mixes 5 and 9, where the applied forces increased from 0.50 kN for Mix 9 to 0.74 kN for Mix 5 (Mix 5 is coarser than Mix 9).

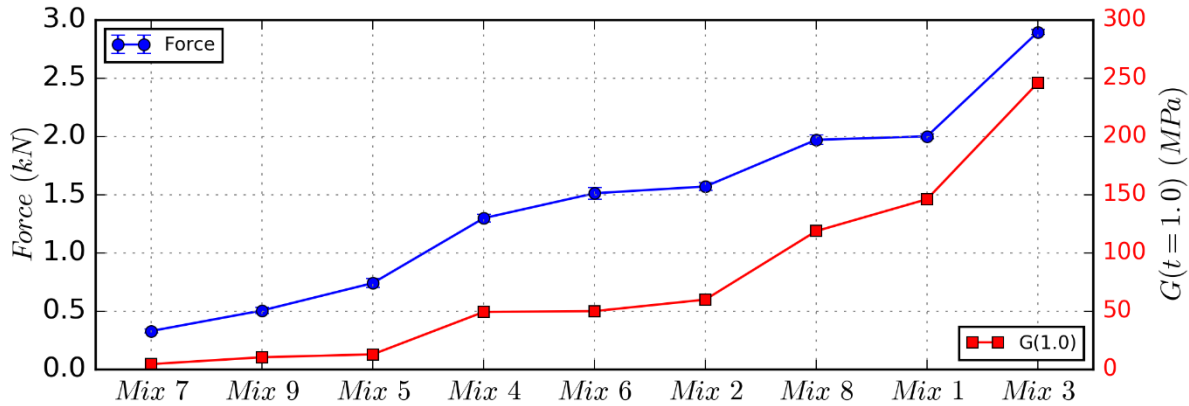


Figure 5-9 Variation of load applied by the loading head and mortar stiffness at $t=1.0$ for each mix.

Crack Opening Strains and Stresses

Stresses and strains in the crack opening direction were plotted along each of the four paths presented in Figure 5-6 and each mix and replicate. Figure 5-10 shows one sample of these plots, which corresponds to the change of the opening strain ϵ_{11} along Path 1 for all the AC mixes. In each plot, the horizontal axis indicates the distance from the center of the notch and the vertical axis of the opening strain. As expected, as the distance from the notch increased from Path 1 to Path 3, the strains decreased. The micromechanical model also predicted a horizontal strain of relevant magnitude in the area around the contact between the loading head and the specimen.

There was not a clear correlation between mortar stiffness and opening strain. However, in general, a low applied load resulted in higher strains. As previously discussed, a low applied load is the consequence of low mortar stiffness resulting in higher crack front strains. This explains the localization of high ϵ_{11} on mortar areas, which had significantly lower stiffness than that of aggregates. A variation of ϵ_{11} along any path shows an area with a magnitude higher than other areas; areas of low strain coincide with aggregate locations, while areas of high strain match mortar zones.

A dependency of strain levels on the replicate number was also observed. For instance, in the first replicate of Mix 5, strain levels reached $20 \times 10^3 \mu\epsilon$. On the other hand, for the third replicate of the same mix, strain levels of $10 \times 10^3 \mu\epsilon$ were obtained. The result implies that aggregate distribution can be as relevant as aggregate gradation itself for the quantification of local crack front parameters such as ϵ_{11} . Aggregate distribution also affected the mix with the highest strains. For the first replicate, Mix 5 had the highest strain levels, but for replicate 2, Mix 7 showed strains along the x -direction with the highest magnitude. This dependency on the aggregate distribution suggests that the strain field is not a reliable indicator of the severity of I-FIT loaded configuration.

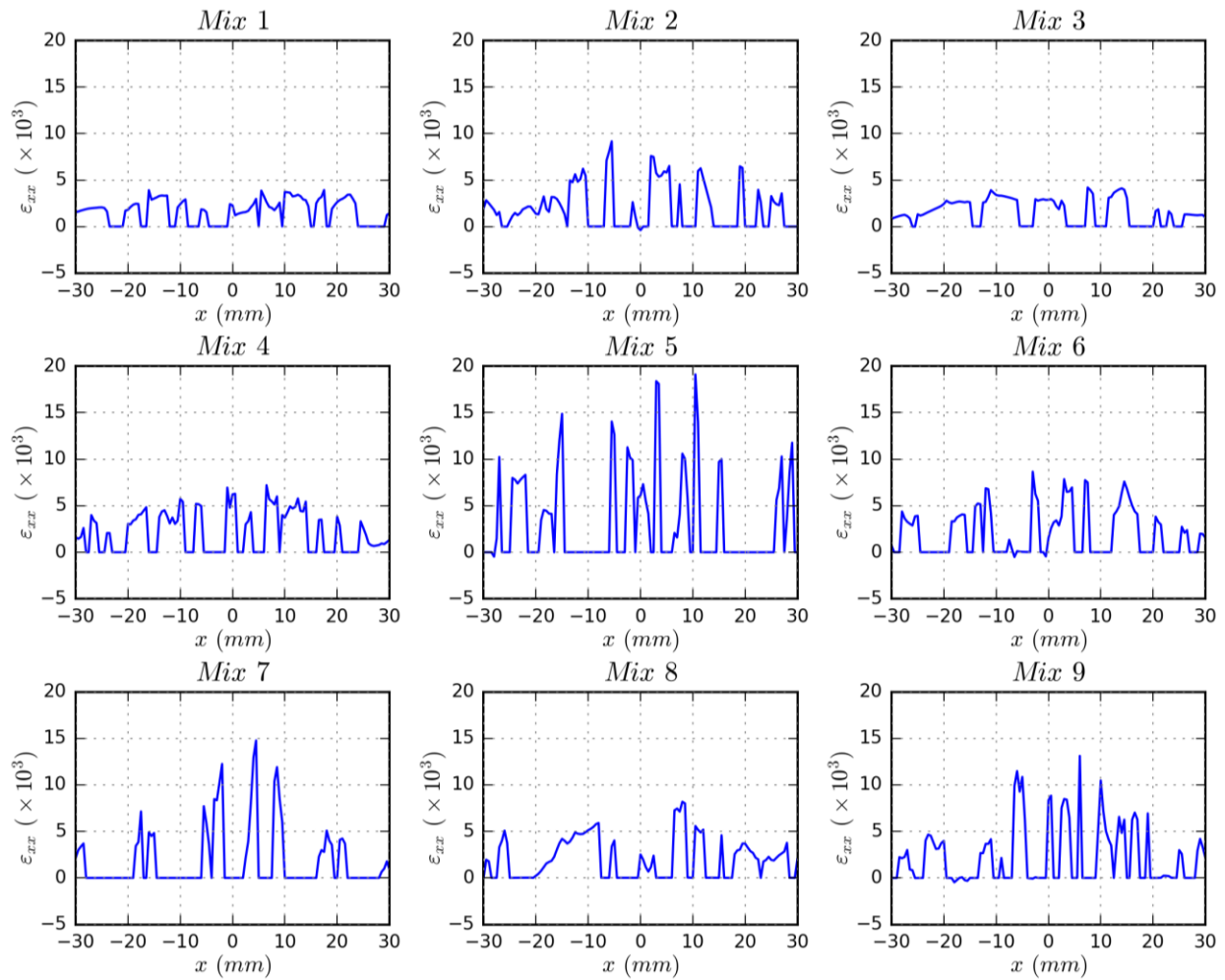


Figure 5-10 Variation of ε_{11} along Path 1 for Replicate 1 in all mixes.

Regarding the opening stresses σ_{11} , Mix 3 and Mix 7 consistently show higher and lower opening stresses for all the replicates, respectively (see Figure 5-11). As shown in Figure 5-9, Mix 3 was subjected to the highest load and contained mortar with the lowest stiffness. On the contrary, the applied force and mortar stiffness were the lowest for Mix 7. The stress levels also suggested a more consistent trend between σ_{11} and the applied force than between ε_{11} and applied force. Finally, the difference in σ_{11} between aggregate and mortar was not as significant as for opening strain.

Energy

The energy term as calculated by Eq. (5.1) for each AC mix is presented in Figure 5-12, along with the stiffness of the mortar at $t=1.0$. The trend is the same as for the applied force, with Mix 3 demonstrating the highest energy, mortar relaxation shear modulus, and applied force and Mix 7 showing the lowest energy, mortar relaxation shear modulus, and applied force. Energy is an indicator of crack driving forces in each AC mix. As the energy increases, crack driving forces

also increases indicating a greater potential for crack initiation and propagation. The mortars with lower relaxation modulus could have a better capability to relax stresses and this results lower energy accumulating at the crack front.

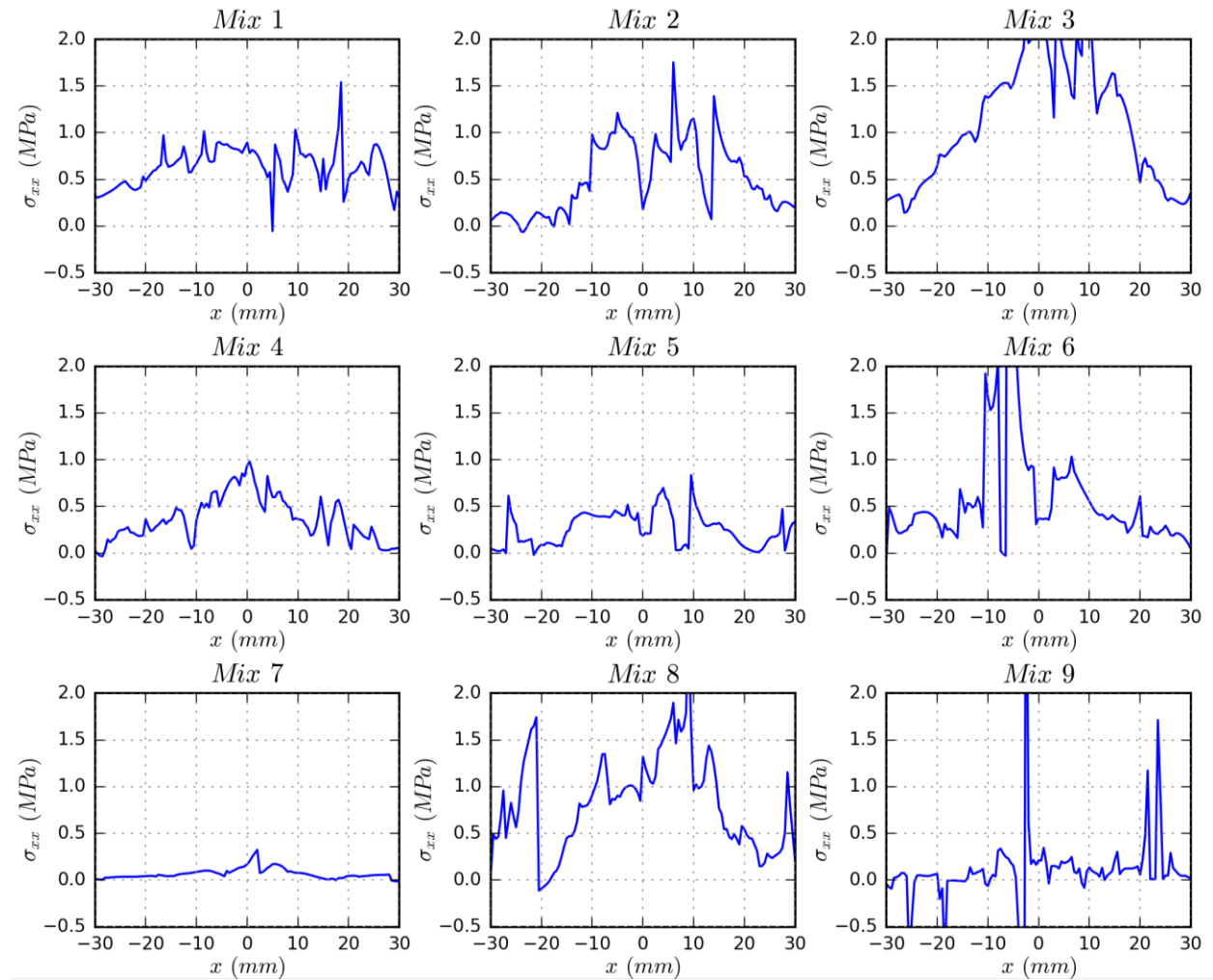


Figure 5-11 Variation of σ_{11} along Path 1 for Replicate 1 in all mixes.

Potential relationships between the energy term, VMA , and percent passing sieve No. 16, P_{16} , were also explored but did not show a similarly correlation trend as it did with $G(t)$. For instance, the energy per unit thickness of Mix 4, with $P_{16}=23.5\%$, was 0.73 N.mm/mm . However, compared with Mix 6, the energy increased to 0.80 N.mm/mm , but P_{16} decreased to 20.0% . Similarly, VMA decreased from 15.3% to 14.5% between Mix 4 and 6. The strong correlation between mortar modulus and energy can be explained by the governing contribution of mortar phase to the energy term as opposed to the aggregates phase. The correlation between the energy and relaxation shear modulus is explained by the encompassing nature of the latter; mortar modulus is influenced by air voids, P_{16} , and binder relaxation modulus.

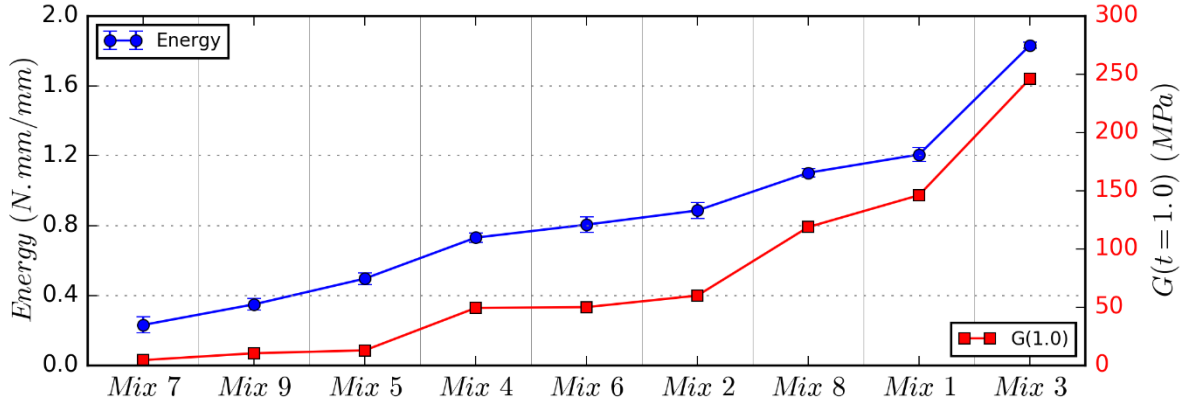


Figure 5-12 Variation of energy term and mortar stiffness at $t=1.0$ for each mix.

5.2.2 Mortar Effect

The effect of mortar on fracture behavior was determined using ten replicates of three of the AC mixes with distinct gradations: Mix 4, 5, and 9. As presented in Table 5-1, VMA for Mixes 4, 5, and 9 are 15.3, 13.8, and 18.5%, respectively. On the other hand, three binders were chosen with properties covering the spectrum from the lowest to highest modulus given in Figure 3-2. The binders were B-6602 RTFO MC, PG 64-22 RTFO, and 2PAV PG64-22 and were labeled Binder 1, 2, and 3, respectively. As in the previous case, the aggregate–mortar interface was defined by $k_x=k_y=1000$ N/mm. The Prony series terms for mortars resulting from the binder–mix combinations are presented in Table 5-2, and Figure 5-13 plots the shear relaxation modulus of each mortar.

Table 5-2. Prony Series Terms for Mortars

ρ_i (sec)	B-6602 RTFO MC			PG64-22 RTFO			2PAV PG64-22		
	M4	M5	M9	M4	M5	M9	M4	M5	M9
1.0×10^{-5}	1.46×10^3	4.76×10^2	4.02×10^2	1.48×10^2	6.61×10^1	6.02×10^1	1.87×10^3	1.22×10^3	1.31×10^3
1.0×10^{-4}	5.64×10^2	1.42×10^2	1.13×10^2	1.32×10^3	4.67×10^2	4.02×10^2	3.42×10^3	1.38×10^3	1.22×10^3
1.0×10^{-3}	3.34×10^2	9.55×10^1	7.87×10^1	1.07×10^3	3.20×10^2	2.64×10^2	7.94×10^2	2.13×10^2	1.74×10^2
1.0×10^{-2}	9.19×10^1	2.14×10^1	1.67×10^1	5.77×10^2	1.60×10^2	1.30×10^2	7.62×10^2	2.45×10^2	2.05×10^2
1.0×10^{-1}	3.47×10^1	1.01×10^1	8.32	2.69×10^2	7.10×10^1	5.73×10^1	4.43×10^2	1.15×10^2	9.28×10^1
1.0	4.04	6.7×10^{-1}	4.6×10^{-1}	7.83×10^1	2.05×10^1	1.66×10^1	2.84×10^2	7.90×10^1	6.45×10^1
1.0×10^1	1.68	5.3×10^{-1}	4.5×10^{-1}	1.87×10^1	4.81	3.86	1.16×10^2	2.91×10^1	2.32×10^1
1.0×10^2	0.0	0.0	0.0	2.90	7.6×10^{-1}	6.2×10^{-1}	4.38×10^1	1.19×10^1	9.69
1.0×10^3	0.0	0.0	0.0	5.6×10^{-1}	1.4×10^{-1}	1.1×10^{-1}	1.11×10^1	2.67	2.12
1.0×10^4	4.9×10^{-3}	0.0	0.0	4.8×10^{-2}	1.4×10^{-2}	1.2×10^{-2}	3.61	1.01	8.2×10^{-1}
1.0×10^4	0.0	0.0	0.0	5.8×10^{-2}	1.5×10^{-2}	1.1×10^{-2}	7.3×10^{-1}	1.7×10^{-1}	1.3×10^{-1}

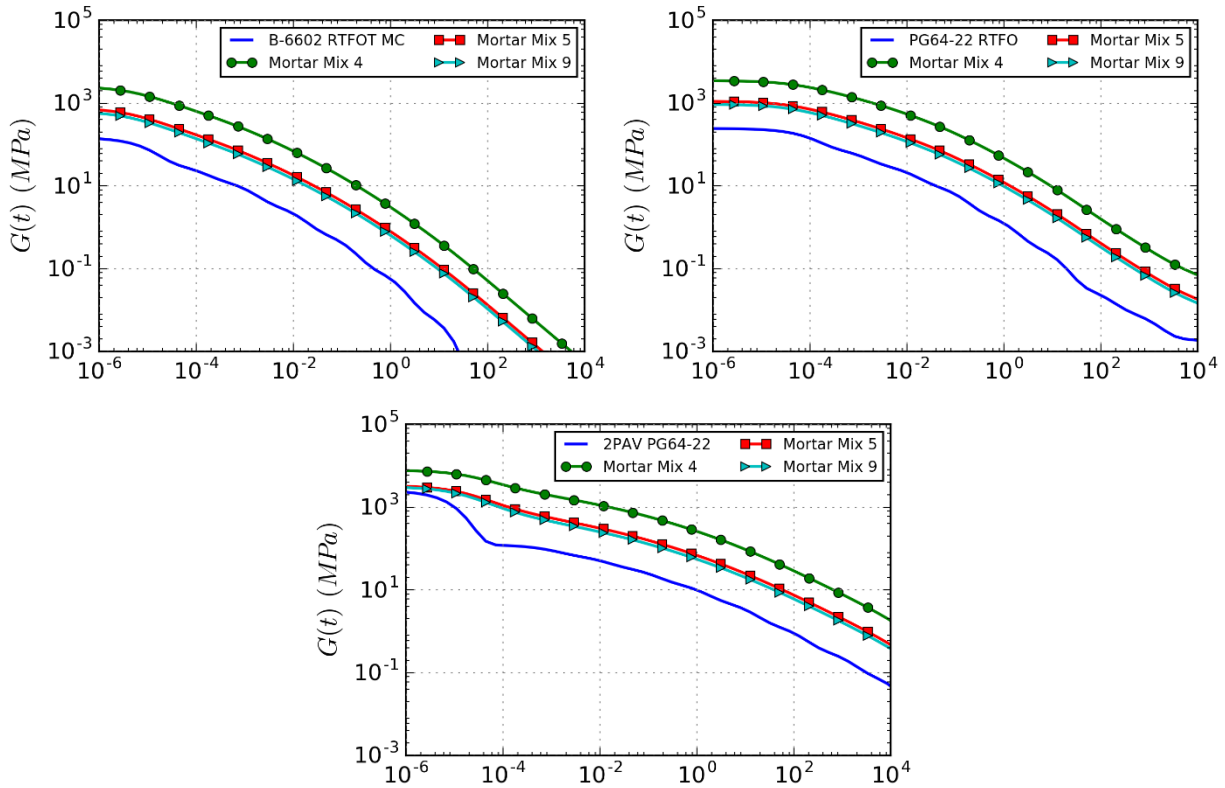


Figure 5-13 Mortar relaxation modulus for the study of binder effect.

Applied Load

The variation of force applied by the loading head F for the binder–mix combinations considered is presented in Figure 5-14, with the horizontal axis representing the mix–binder combination (e.g., $M5B2$ indicates Mix 5 with Binder 2). The applied force increased as $G(t)$ became greater, with the highest magnitude observed for Mix 4 with Binder 3 (3.14 kN) and the lowest for Mix 9 with Binder 1 (0.08 kN). In general, the samples using stiffer binder provided a higher applied force regardless of the mix type as can be inferred from the ranking presented in Figure 5-14, where the three forces for Binder 3 were on the right portion of the plot, as compared with Binder 1 where the forces were on the left region.

Figure 5-14 also highlights the influence of gradation on the applied force. First, the rate of the increment in the applied force with respect to the binder was higher for Mix 4, followed by Mix 5 and Mix 9. For instance, the difference between the highest and lowest F is 2.89 kN in Mix 4 and 1.32 kN in Mix 9. Second, as the mortar becomes stiffer, the mixes became more sensitive to gradation changes with an increase in applied load from M9 to M4. Third, as shown in Figure 5-13, the difference in $G(t)$ between Mixes 5 and 9 was minimal, but the narrow discrepancy in shear relaxation modulus did not translate into a slight difference in applied force. In the particular case of Binder 2, the shear relaxation modulus at $t=1.0$ increased from 10.3 MPa for Mix 9 to 12.8 MPa Mix 5, a 25% increment. On the other hand, F increased 60% from 0.50 kN to 0.77 kN.

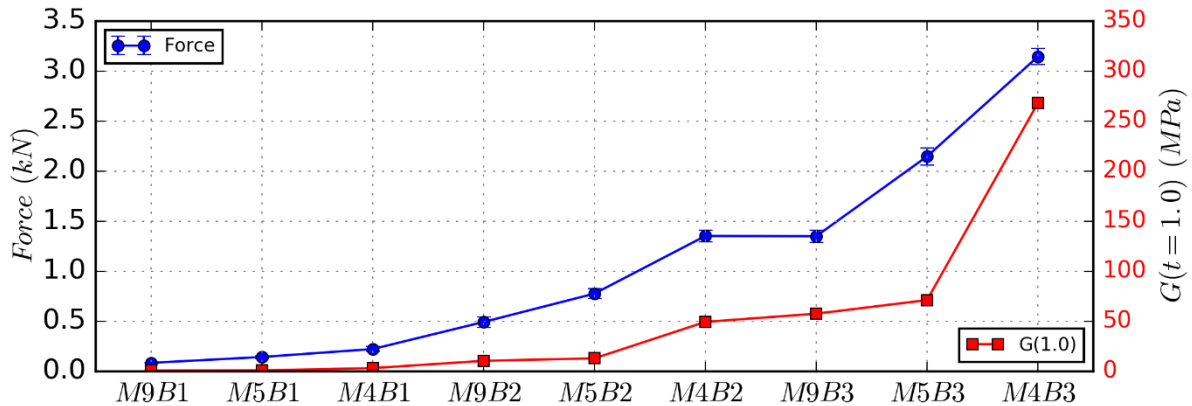


Figure 5-14. Variation of applied force with binder type for Mixes 4, 5, and 9.

Opening Strains and Stresses

The variation of ε_{11} along Paths 1-4 did not show a clear trend for strains and stresses by changing binder properties and mixture. For instance, for Mix 4 and Replicates 1, 2, and 4, the strain levels decreased as binder stiffness increased; however, that is not the case for Replicate 3. Similarly, for Replicate 4 of Mix 9, the strain levels decreased with binder stiffness, but strain levels increased from Binder 1 to Binder 2 and decreased from Binder 2 to Binder 3 for the other mixes.

Even though minimal variability was observed in the applied force, a relatively high dissimilarity in strain levels was identified between replicates. For example, Mix 5 with Binder 1 and Replicate 1 exhibited strains of around 15000 $\mu\varepsilon$; Replicate 3 showed strains between 5000 and 10000 $\mu\varepsilon$; and Replicate 4 indicated strains less than 5000 $\mu\varepsilon$. As in the previous section, the variation of opening strains along Paths 1 through 4 proved to be an unreliable output for assessing the loaded configuration of an I-FIT sample. This may be due to poor statistical representation of a single path chosen at the crack front due to high heterogeneity where local fields (stresses and strains) govern. Therefore, more emphasis was given to energy-like terms and global terms (applied load) as they are more representative of crack front volume or the entire specimen.

On the other hand, opening stresses showed a close relationship with the shear relaxation modulus: the highest stresses were seen in Mix 4 with Binder 3, and the lowest for Mix 9 with Binder 1 in all the replicates. This trend also matches the relation between reaction force and relaxation shear modulus.

Energy

Figure 5-15 and Figure 5-16 present the variation of energy, applied force, and mortar relaxation shear modulus for each mix–binder combination. Energy, mortar shear relaxation modulus, and reaction force showed a strong correlation to one another. Mix 4 stored the most energy, with the

highest magnitude seen in the combination of Mix 4 and Binder 3. As showed in Figure 5-16, the lines for the energy and applied force are almost parallel, indicating an even stronger relation between one another.

Unlike the opening stresses and strains, there was very little variation among the replicates describing the relationship between the energy and the mortar modulus. It should be noted that mortar modulus considered the *VMA*, the binder modulus, and P_{16} .

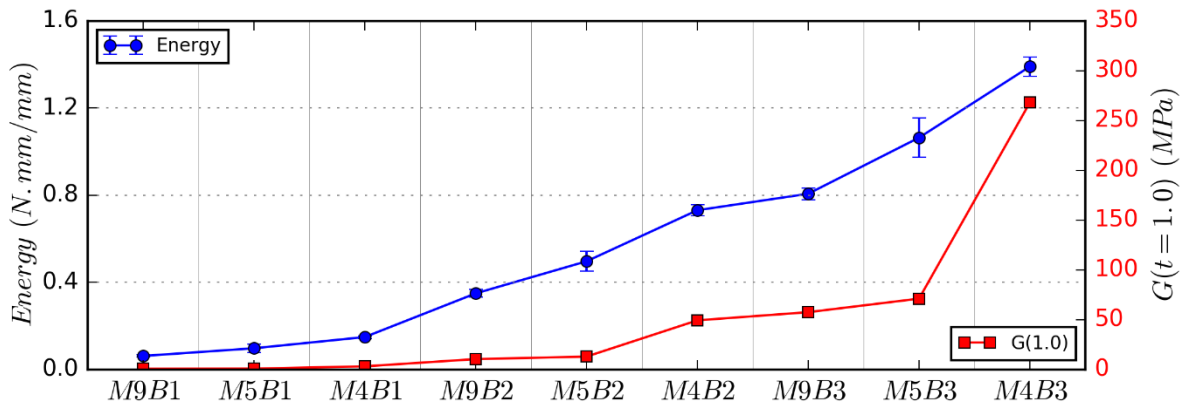


Figure 5-15 Variation of energy term and mortar stiffness at $t=1.0$ for each mix-binder combinations.

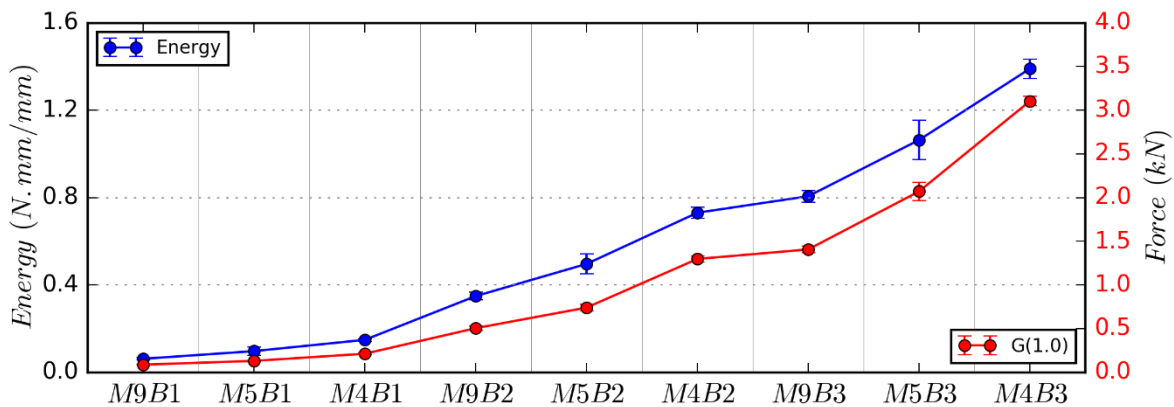


Figure 5-16. Variation of energy term and applied force for each mix-binder combinations.

5.3 DESIGN CONSIDERATIONS

Table 5-3 shows a summary of the results for average energy and force. As previously mentioned, a direct link between these outputs and specific AC mix design variables (e.g., VMA and binder content) could not be found. However, force and energy correlated well with mortar modulus.

It should also be highlighted that values in Table 5-3 indicate demand imposed on the material. The other side of the design equation, the material capacity, can be established by the fracture energy. The demand–capacity ratio is more important than the magnitude of one of the two separately. For instance, on one hand, the total energy applied on the I-FIT specimen can be obtained from ABAQUS, which is 725.9 N-mm for Mix 2-Replicate 1 and 1510.6 N-mm for Mix 3-Replicate 1. On the other hand, the capacity can be computed using fracture energy. The fracture is defined as the area under the load–deflection curve divided by ligament area. For Mix 2 and 3, the fracture energy was measured as 1874.7 J/m² and 2202.9 J/m², respectively. Considering a ligament area of 0.003 m², the area under the load–deflection curve is 5624.1 and 6608.7 N-mm for Mix 2 and 3, respectively. The demand–capacity ratio for Mix 2 is 13.5% and for Mix 3 is 22.9%; consequently, Mix 3 is more likely to fail than Mix 2.

Table 5-3. Summary of Energy and Force for the Various Mix–Binder Combinations

Binder	Mix	Force (kN)	Energy (N.mm/mm)
B1	M9	0.087	0.062
	M5	0.130	0.097
	M4	0.212	0.148
B2	M9	0.504	0.349
	M5	0.740	0.496
	M4	1.297	0.730
B3	M9	1.406	0.806
	M5	2.070	1.063
	M4	3.104	1.390
B2	M7	0.328	0.231
	M9	0.504	0.349
	M5	0.740	0.496
	M4	1.297	0.730
	M6	1.511	0.805
	M2	1.569	0.886
	M8	1.970	1.102
	M1	2.000	1.206
	M3	2.895	1.831

CHAPTER 6 - CONCLUSIONS AND RECOMMENDATIONS

The main objective of this study was to propose a link between the fracture properties of asphalt concrete (AC) and overlay analysis and design. In order to accomplish this goal, numerical models of a commonly used fracture Illinois-Flexibility Index Test (I-FIT) were developed. A 2-D micromechanical model of I-FIT geometry was generated and validated using images of actual specimens as well as the computer-generated microstructures and digital image correlation (DIC). Using a micromechanical finite element (FE) model, several AC mix designs were analyzed covering a wide range of gradations and binder properties. Various replicates of the same AC mix design were created using Python-based script, and responses such as applied force, stresses, strains, and energy were studied. The following findings summarize the outcome of this study:

- Micromechanical I-FIT model consisted of mortar and aggregate phases in addition to nonlinear springs between the two phases. The spring coefficient was determined to be 1000 N/mm and verified by sensitivity analysis.
- Micromechanical model was validated by the results obtained from a DIC test on the same test specimen. The results showed that acceptable agreement can be obtained with no calibration.
- According to the parametric study conducted by computer-generated images of various mixes, energy and applied force showed a great correlation with mortar stiffness. Other volumetric and material variables such as voids in the mineral aggregate (*VMA*) and binder stiffness did not display trends with such high correlation.
- The influence of air voids, binder stiffness, and fine aggregate on fracture performance cannot be studied separately. On the contrary, mortar stiffness is a better alternative because it couples the effect of the mentioned parameters in a single variable. Mortar properties governed the fracture response.
- Stresses and strains along a single path at the crack front are not reliable criteria for assessing the fracture behavior of AC because their magnitude depends on the aggregate distribution. In other words, the same AC mix design with the same material properties can provide a very different stress/strain field due to different aggregate distribution.
- The effect of applied load on opening stress was more consistent than the opening strains. In addition, the difference in stresses between aggregates and mortar was smaller than the discrepancy in strains.
- A direct link between mix design variables such as *VMA* and binder content and I-FIT responses could not be found. However, energy and applied load correlated well with mortar modulus.

The study also concludes the following:

- The numerical model developed for fracture I-FIT was sufficiently accurate and validated by using micromechanical modeling.
- The link between I-FIT test and overlay analysis/design should be based on energy rather than specific volumetric or material properties.

REFERENCES

- Abanto-Bueno, J., & Lambros, J. (2002). Investigation of Crack Growth in Functionally Graded Materials Using Digital Image Correlation. *Engineering Fracture Mechanics*, 69(14), 1695-1711.
- Abu Abdo, A. M., Eckwright, F., Jung, S. J., Bayomy, F., & Nielsen, R. (2014, February). Semi-circular Notched Beam Testing Procedure for Hot Mixture Asphalt. In *Proceedings of the Institution of Civil Engineers-Transport* (Vol. 167, No. 1, pp. 48-58). Thomas Telford Ltd.
- Aliha, M. R. M., Fazaeli, H., Aghajani, S., & Nejad, F. M. (2015). Effect of Temperature and Air Void on Mixed Mode Fracture Toughness of Modified Asphalt Mixtures. *Construction and Building Materials*, 95, 545-555.
- Aliha, M. R. M., Ameri, M., Mansourian, A., & Ayatollahi, M. R. (2012). Finite Element Analysis of a New Test Specimen for Investigating Mixed Mode Cracks in Asphalt Overlays. In *7th RILEM International Conference on Cracking in Pavements* (pp. 359-367). Springer Netherlands.
- Al-Qadi, I. L., Elseifi, M., & Leonard, D. (2003). Development of an Overlay Design Model for Reflective Cracking with and without Steel Reinforcing Nettings. *Asphalt Paving Technology*, 72, 388-423.
- Al-Qadi, I. L., Aurangzeb, Q., Carpenter, S. H., Pine, W. J., & Trepanier, J. (2012). Impact of High RAP Contents on Structural and Performance Properties of Asphalt Mixtures. *FHWA-ICT-12-002*.
- Al-Qadi, I. L., Ozer, H., Lambros, J., El Khatib, A., Singhvi, P., Khan, T., Rivera-Perez, J & Doll, B. (2015). *Testing Protocols to Ensure Performance of High Asphalt Binder Replacement Mixes Using RAP and RAS*. Illinois Center for Transportation/Illinois Department of Transportation.
- Al-Qadi, I. L., Son, S., & Carpenter, S. H. (2013). Development of an Economical, Thin, Quiet, Long-Lasting, High Friction Surface Layer, Volume 1: Mix Design and Lab Performance Testing. *FHWA-ICT-13-001*.
- American Association of State Highway, & Transportation Officials (AASHTO). (1993). *AASHTO Guide for Design of Pavement Structures, 1993* (Vol. 1). AASHTO.
- American Association of State Highway and Transportation Officials (AASHTO). 1997. "Segregation: Causes and Cures for Hot Mix Asphalt." Publication by the Joint Task Force on Segregation of AASHTO Subcommittees on Construction and Materials, and National Asphalt Pavement Association, Washington, D.C.
- American Association of State Highway and Transportation Officials (AASHTO). (2016). "Determining the Fracture Potential of Asphalt Mixtures Using the Flexibility Index Test (FIT)"
- Aragão, F., Hartmann, D., Kim, Y. R., da Motta, L., & Haft-Javaherian, M. (2014). Numerical-Experimental Approach to Characterize Fracture Properties of Asphalt Mixtures at Low Temperatures. *Transportation Research Record: Journal of the Transportation Research Board*, (2447), 42-50.
- ASCE, Report card for America's Infrastructure, American Society of Civil Engineers, Reston, VA. Available online at <http://www.infrastructurereportcard.org> (accessed May 2017).
- Asphalt Institute (AI). (2000). Asphalt Overlay for Highway and Street Rehabilitation. *Manual Series*, 17.

- Ameri, M., Mansourian, A., Pirmohammad, S., Aliha, M. R. M., & Ayatollahi, M. R. (2012). Mixed Mode Fracture Resistance of Asphalt Concrete Mixtures. *Engineering Fracture Mechanics*, 93, 153-167.
- Amirkhanian, S. M., & Putnam, B. J. (2006). *Laboratory and field investigation of temperature differential in HMA mixtures using an infrared camera* (No. FHWA-SC-06-06). Clemson University Department of Civil Engineering.
- Artamendi, I., & Khalid, H. A. (2006). A Comparison between Beam and Semi-Circular Bending Fracture Tests for Asphalt. *Road Materials and Pavement Design*, 7(sup1), 163-180.
- Barber, E. (2016). Impact Of Testing Variability On Asphalt Concrete Fracture Potential. Master Thesis, Politecnico Di Milan.
- Buttlar, W. G., Hill, B. C., Kim, Y. R., Kutay, M. E., Millien, A., Montepara, A., & Roncella, R. (2014). Digital Image Correlation Techniques to Investigate Strain Fields and Cracking Phenomena in Asphalt Materials. *Materials and structures*, 47(8), 1373-1390.
- Bruck, H. A., McNeill, S. R., Sutton, M. A., & Peters, W. H. (1989). Digital Image Correlation Using Newton-Raphson Method of Partial Differential Correction. *Experimental mechanics*, 29(3), 261-267.
- Brock, J. D. (1986). Segregation of asphaltic mixtures. In *Proceedings of the Association of Asphalt Paving Technologists* (Vol. 55, pp. 269-277).
- Carroll, J. D., Abuzaid, W., Lambros, J., & Sehitoglu, H. (2013). High Resolution Digital Image Correlation Measurements of Strain Accumulation in Fatigue Crack Growth. *International Journal of Fatigue*, 57, 140-150.
- Chu, T. C., Ranson, W. F., & Sutton, M. A. (1985). Applications of Digital-Image-Correlation Techniques to Experimental Mechanics. *Experimental mechanics*, 25(3), 232-244.
- Collop, A. C., & Cebon, D. (1995). A Theoretical Analysis of Fatigue Cracking in Flexible Pavements. *Proceedings of the Institution of Mechanical Engineers, Part C: Journal of Mechanical Engineering Science*, 209(5), 345-361.
- Doll, B., Ozer, H., Rivera-Perez, J. J., Al-Qadi, I. L., & Lambros, J. (2017). Investigation of Viscoelastic Fracture Fields in Asphalt Mixtures Using Digital Image Correlation. *International Journal of Fracture*, 205(1), 37-56.
- Elseifi, M. A., Mohammad, L. N., Ying, H., & Cooper III, S. (2012). Modeling and Evaluation of the Cracking Resistance of Asphalt Mixtures Using the Semi-circular Bending Test at Intermediate Temperatures. *Road Materials and Pavement Design*, 13(sup1), 124-139.
- Ghauch, Z. G., Ozer, H., & Al-Qadi, I. L. (2015). Micromechanical Finite Element Modeling of Moisture Damage in Bituminous Composite Materials. *Construction and Building Materials*, 80, 9-17.
- Huang, B., Shu, X., & Zuo, G. (2013). Using Notched Semi-Circular Bending Fatigue Test to Characterize Fracture Resistance of Asphalt Mixtures. *Engineering Fracture Mechanics*, 109, 78-88.
- Kim, Y. R., & Little, D. N. (2004). Linear Viscoelastic Analysis of Asphalt Mastics. *Journal of Materials in Civil Engineering*, 16(2), 122-132.
- Kim, M., Mohammad, L., & Elseifi, M. (2012). Characterization of Fracture Properties of Asphalt Mixtures as Measured by Semi-Circular Bend Test and Indirect Tension Test. *Transportation Research Record: Journal of the Transportation Research Board*, (2296), 115-124.
- Leclerc, H., Périé, J. N., Roux, S., & Hild, F. (2009, May). Integrated Digital Image Correlation For The Identification Of Mechanical Properties. In *International Conference on*

- Computer Vision/Computer Graphics Collaboration Techniques and Applications* (pp. 161-171). Springer Berlin Heidelberg.
- Li, G., Li, Y., Metcalf, J. B., & Pang, S. S. (1999). Elastic Modulus Prediction of Asphalt Concrete. *Journal of Materials in Civil Engineering*, 11(3), 236-241.
- Li, X., & Marasteanu, M. O. (2006). The Role of Temperature and Binder Type on the Fracture Resistance of Asphalt Mixtures at Low Temperatures. *Road Materials and Pavement Design*, 7(3), 331-348.
- Li, X., Braham, A. F., Marasteanu, M. O., Buttlar, W. G., & Williams, R. C. (2008). Effect of Factors Affecting Fracture Energy of Asphalt Concrete at Low Temperature. *Road Materials and Pavement Design*, 9(sup1), 397-416.
- Li, X. J., & Marasteanu, M. O. (2010). Using Semi Circular Bending Test to Evaluate Low Temperature Fracture Resistance for Asphalt Concrete. *Experimental Mechanics*, 50(7), 867-876.
- Lim, I. L., Johnston, I. W., & Choi, S. K. (1993). Stress Intensity Factors for Semi-circular Specimens under Three-Point Bending. *Engineering Fracture Mechanics*, 44(3), 363-382.
- Lippert, D. L., Wu, S., Ozer, H., Al-Qadi, I. L., Meister, J. F., Renshaw, G., Barry, M., Said, I., Espinoza Luque, A., & Safi, F. (2017). Construction and Performance Monitoring of Various Asphalt Mixes in Illinois: 2016 Interim Report. Illinois Center for Transportation/Illinois Department of Transportation.
- Mohammad, L. N., Kabir, M. D., & Saadeh, S. (2008, June). Evaluation of Fracture Properties of Hot Mix Asphalt. In *Proceedings of the 6th RILEM International Conference on Cracking in Pavements, Chicago, Illinois* (pp. 427-436).
- National Cooperative Highway Research Program (NCHRP). (2004). "Guide for the Mechanistic-Empirical Design for New and Rehabilitated Pavement Structures." I-37A, Washington, DC.
- Newcomb, D. E. (2009). Thin Asphalt Overlays for Pavement Preservation (No. Information Series 135).
- Ozer, H., Al-Qadi, I. L., Singhvi, P., Khan, T., Rivera-Perez, J., & El Khatib, A. (2016). Fracture Characterization of Asphalt Mixtures With High Recycled Content Using Illinois Semicircular Bending Test Method and Flexibility Index. *Transportation Research Record: Journal of the Transportation Research Board*, (2575), 130-137.
- Ozer, H., Al-Qadi, I. L., Lambros, J., El Khatib, A., Singhvi, P., & Doll, B. (2016). Development of the Fracture-Based Flexibility Index for Asphalt Concrete Cracking Potential Using Modified Semi-Circle Bending Test Parameters. *Construction and Building Materials*, 115, 390-401.
- Ozer, H., Al-Qadi, I. L., Singhvi, P., Bausano, J., Carvalho, R., Li, X., & Gibson, N. (2018). Assessment of Asphalt Mixture Performance Tests to Predict Fatigue Cracking in an Accelerated Pavement Testing Trial. *International Journal of Pavement Engineering, Special Issue for Cracking in Flexible Pavements and Asphalt Mixtures: Theories to Modeling, and Testing to Mitigation*.
- Pirmohammad, S., & Ayatollahi, M. R. (2014). Fracture Resistance of Asphalt Concrete under Different Loading Modes and Temperature Conditions. *Construction and Building Materials*, 53, 235-242.

- Saha, G., & Biligiri, K. P. (2015). Fracture Damage Evaluation of Asphalt Mixtures Using Semi-circular Bending Test Based on Fracture Energy Approach. *Engineering Fracture Mechanics*, 142, 154-169.
- Saha, G., & Biligiri, K. P. (2016). Fracture Properties of Asphalt Mixtures Using Semi-circular Bending Test: A State-of-the-Art Review and Future Research. *Construction and Building Materials*, 105, 103-112.
- Sawalha, M., Ozer, H., Al-Qadi, I. L., & Xue, H. (2017). Development of a Modified Adhesion Test for Hot-Poured Asphalt Crack Sealants. *Transportation Research Record: Journal of the Transportation Research Board*, (2612), 85-95.
- Schapery, R. A. (1962, June). Approximate Methods of Transform Inversion for Viscoelastic Stress Analysis. In *Proc. 4th US National Congress of Applied Mechanics* (Vol. 2)
- Sharma, B. K., Ma, J., Kunwar, B., Singhvi, P., Ozer, H., & Rajagopalan, N. (2017). *Modeling the Performance Properties of RAS and RAP Blended Asphalt Mixes Using Chemical Compositional Information* (No. FHWA-ICT-17-001).
- Shu, X., & Huang, B. (2008a). Dynamic Modulus Prediction of HMA Mixtures Based on the Viscoelastic Micromechanical Model. *Journal of Materials in Civil Engineering*, 20(8), 530-538.
- Shu, X., & Huang, B. (2008b). Micromechanics-based Dynamic Modulus Prediction of Polymeric Asphalt Concrete Mixtures. *Composites Part B: Engineering*, 39(4), 704-713.
- Kozicki, J., & Tejchman, J. (2013). Application of DIC Technique to Concrete—Study on Objectivity of Measured Surface Displacements. *Experimental Mechanics*, 53(9), 1545-1559.
- Sousa, J. B., Pais, J. C., & Way, G. B. (2005). A Mechanistic-empirical Based Overlay Design Method for Reflective Cracking. *Road materials and pavement design*, 6(3), 339-363.
- Sousa, J., Pais, J., Saim, R., Way, G., & Stubstad, R. (2002). Mechanistic-empirical Overlay Design Method for Reflective Cracking. *Transportation Research Record: Journal of the Transportation Research Board*, (1809), 209-217.
- Sutton, M. A., Orteu, J. J., & Schreier, H. (2009). *Image Correlation for Shape, Motion and Deformation Measurements: Basic Concepts, Theory and Applications*. Springer Science & Business Media.
- Wu, Z., Rong, H., Zheng, J., Xu, F., & Dong, W. (2011). An Experimental Investigation on the FPZ Properties in Concrete Using Digital Image Correlation Technique. *Engineering Fracture Mechanics*, 78(17), 2978-2990.
- You, T., Im, S., Kim, Y. R., & Little, D. N. (2016). Mechanistic Modeling to Evaluate Structural Performance of Bituminous Pavements with Inelastic Deformation and Fatigue Damage of Mixtures. *Journal of Engineering Mechanics*, 04016126.